Aspects on Wind Turbine Protections and Induction Machine Fault Current Prediction

Marcus Helmer

Department of Electric Power Engineering
CHALMERS UNIVERSITY OF TECHNOLOGY
Göteborg, Sweden 2004

THESIS FOR THE DEGREE OF LICENTIATE OF ENGINEERING

Aspects on Wind Turbine Protections and Induction Machine Fault Current Prediction

Marcus Helmer

Department of Electric Power Engineering
CHALMERS UNIVERSITY OF TECHNOLOGY
Göteborg, Sweden 2004

Aspects on Wind Turbine Protections and Induction Machine Fault Current Prediction

Marcus Helmer

Technical Report No. 516L
ISSN 1651-4998
Department of Power Electronics and Motion Control
School of Electrical Engineering
CHALMERS UNIVERSITY OF TECHNOLOGY
SE-412 96 Göteborg
Sweden
Telephone + 46 (0)31 772 1000

Chalmers bibliotek, Reproservice
Göteborg, Sweden 2004

Abstract

This thesis presents detailed modelling of the induction machine with the main objective being accurate fault current prediction. The thesis focuses mainly on mains connected induction machines and the response due to severe disturbances in the supply voltage, such as three-phase short circuit faults. Both the squirrel-cage induction machine as well as the doubly-fed induction machine are treated.

In order to accomplish accurate results, dynamic parameters of the induction machine is needed, and accordingly, extensive measurement series has been accomplished in order to identify these. A large number of locked-rotor tests and no-load tests with varying voltages and frequencies have been performed to find out the varying nature of the parameters due to skin effect and saturation of the leakage flux path.

To incorporate for the skin effect and the effect of leakage flux path saturation in the calculations, a conventional dynamic mathematical description of the induction machine (5^{th} order Park model) is modified, which makes it applicable for various operating conditions. The fault current prediction of the detailed model is compared with the prediction of the conventional fifth order model and a dynamically equivalent three-phase model, and also with measurements of symmetrical and asymmetrical short circuit faults, starts and locked-rotor tests.

The proposed model show excellent agreement, and also indicates the essentiality to incorporate for the saturation of the leakage flux path and the skin effect as the response due to severe faults is to be determined and if a high accuracy result is the objective. Incorporation of the main flux saturation however, is of little importance for the short-circuit fault currents.

Regarding the selection of a two- or three phase model, the most appropriate model as well as the more simple model, is generally the two-axis model. The disadvantage is the inability to account for a zero sequence component. The possible choice of using a three phase model is however only an issue if the generator is wye connected and if the neutral point of the generator is connected. Wind turbine generators are mainly connected in delta which imply no neutral point and if they are connected in wye, the neural point is however not connected.

In the thesis the fault current determination for the doubly-fed induction generator system and the fixed-speed system are treated. The fault current determination for the full power converter system is however not dealt with since this type of system have full control of the fault currents and can control these to a desired level.

Acknowledgement

This work has been carried out at the Department of Electric Power Engineering at Chalmers University of Technology. The financial support provided by Energimyndigheten (Vindforsk) och ELFORSK is gratefully acknowledged.

Assoc. Prof. Torbjörn Thiringer, thank you for your help, encouragement and engagement. Without his encouraging and inspiring attitude I believe that it would have been impossible to finish this work. Moreover, thanks to Docent Ola Carlson, who introduced me to field of electric power engineering and to my supervisor of that time, Dr. Åke Larsson. I also would like to send a special thanks to my examiner Prof. Tore Underland for inspiring me to complete this thesis.

Finally, I would like to thank all my colleges at the department of Electric Power Engineering.

To my Family

Contents

Chapter 1

Introduction

The wind energy area is developing rapidly and questions are raised regarding the effects of a high level of penetration of wind power into the electrical system. Not only are the wind turbines becoming larger but are also often put up in groups, *wind farms*. The interference with the electrical grid is thus becoming more important, compared to the interference of one single wind turbine. Wind farms can in some cases provide the electrical grid with a significant part of the total energy production, with respect to other energy production units within a certain area. It is therefore important to consider the energy balance both locally, regionally and globally. For instance, a disconnection of an entire wind farm due to a disturbance may lead to a local power deficit, overloading of adjacent lines and a chain-reaction of production and lines being taken out of operation. It is thus of great importance that disconnection of wind turbines only take place if it is absolutely necessary.

Network disturbances are often related to faults to some extent. The most common faults are single phase earth faults [12], but a three-phase short circuit fault are however considered to be the most severe fault condition and are therefore the dimensioning case, both thermally and mechanically. Since the generator is one of the key components in a wind energy conversion system (WECS), it is accordingly important to be aware of the generator and its behavior with respect to different types of faults or disturbances.

Demands by the utilities of additional external protections for wind turbines are becoming more and more common. The reason is, that control centers desires the possibility to take the wind turbines out of operation in case that is a necessity, i.e. to ensure that the wind turbines are disconnected from the main electrical grid due to severe faults (to ensure proper selectivity) but also to provide protection against secondary faults and for personal safety reasons.

A large amount of wind power connected to a point in the electrical grid, may affect the direction and the magnitude of the fault currents, having consequences on the settings of the existing electrical protections, which is one reason to consider the

dynamic behavior of the wind turbine generators. Another reason is the design of substations, in which the peak short circuit currents are an important factor. The peak short-circuit current is the mechanically dimensioning parameter and must of course be considered as new installations of wind turbines are made.

1.1 Review of Related Research

There are two different subjects which has been considered for the review of the related research, *wind turbine protection* and *induction machine modelling*, where the area of wind turbine protection is secondary.

The area of wind turbine protection is rather uninvestigated in the contrary to the area of dynamic modelling of the induction machine, which is very well covered. There exist numerous papers, and thus a review of relevant published material within the area of induction machine modelling is of great interest. The area of wind turbine protection has been investigated by [7] to some extent, but deals mainly with the protection of entire wind farms. In this thesis however, the protection system of wind turbines are used as a perspective when it comes to generator modelling.

The induction machine is widely used in various electrical drives. According to [22], about 70 % of the industrial load is represented by induction machines. In [4] a figure of 40-60 % is mentioned, but it is also stated that the induction machine load, in some cases, could be up to 90 % of the total load. Hence, the need for high accuracy induction machine models, in order to predict the fault current contribution in to the grid, is great [15].

When short circuit calculations are performed, the fault current contribution from induction machines is often neglected [4]. However, the author presents calculations of the short circuit current using the standard Park model [17] and a comparison with the result from simple analytical calculations and finally comes to the conclusion, that the Park model should be used for short circuit calculations if there is a significant amount of induction machines present. In [22] calculations of short circuit currents using the traditional Park model are compared with measurements. The comparison is done for one phase current and a discrepancy + 20 % and - 20 % between the two cases presented is found.

The Park model is a useful tool, but one has have to use various sets of parameters for accurate prediction of the currents, with respect to different operating conditions. The importance of a correct set of parameter is stressed further as transient processes are analyzed. It is not very convenient to shift model parameters and a more convenient solution would be to use one model, which can be used for steady state operation as well as when the machine is subjected to severe disturbances. In [15] a method to achieve this is presented. The parameters are determined as a function of the slip. However,

this is basically a steady state adjustment, and is not quite correct for transient analysis, since the current and speed in reality changes with different time scales.

There are several theoretical papers on the subject of advanced dynamic modelling of the induction machine. More advanced models of the induction machine has been developed by [16] and [18], where models including the skin effect and the saturation of the main- and leakage flux path is presented. The incorporation of the main flux saturation was first proposed in [21], but for dynamic analysis of grid connected induction machines this is claimed to be of minor importance [20], especially for transient conditions [16].

The saturation of the leakage flux path and the skin effect in the rotor conductors are however, of greater importance for transient analysis. The skin effect phenomenon in transient analysis is emphasized in [8] and in [2] a double cage rotor configuration in order to account for the skin effect is suggested.

However, a paper comparing the results of short circuit measurements with calculations, using a model taking the skin effect in the rotor conductors and the saturation of the leakage flux path into account, has not been found by the author.

1.2 The Aim of the Thesis

The purpose of this thesis is on one hand to enlighten the reader on different aspects of protection of the wind power establishment, WPE, and to investigate the model requirement for fault current prediction. The protection system of a wind farm is an interesting issue and is discussed to some extent. However, the thesis deals mainly with the response of the short circuited induction generator due to abnormal operating conditions, i.e. heavy electrical fault conditions such as short circuit faults, where both symmetrical and unsymmetrical conditions are considered.

The thesis considers the fixed speed system and the doubly-fed induction generator system, while the full power converter system is left out. The reason is that the response of the electrical generating system for the full power converter system is fully controllable, while the response of the fixed-speed generating system is not at all controllable. For the doubly-fed induction generator system they are only controllable for minor grid disturbances.

Chapter 2

Wind Turbine Operation

2.1 Wind Energy Conversion Systems - WECS

From an electrical point of view, the wind turbines are often divided into either fixed-speed wind turbines or variable-speed wind turbines. The generally used systems of the latter consists of either a synchronous generator, where a converter is connected to the generator stator side or a doubly-fed induction generator (DFIG), which imply that the converter is connected to the rotor circuit of the generator and that the stator is connected directly to the electrical grid. In the fixed speed system, the generator is connected directly to the electrical grid. The variable speed system is becoming the more common type nowadays, since it comprise a greater possibility in controlling the output active power as well as the reactive power flow. And today (2004) all turbines larger than 2.5 MW are of variable speed type. The main advantage of the variable speed system is the lower stresses on the mechanical construction, which follows due to the possibility to control the shaft torque of the turbine. The fixed-speed wind turbines however, represent a large part of the existing wind turbines and are today still successfully produced up to a size of 2MW.

2.1.1 Fixed Speed System

The electrical system in a fixed-speed wind turbine consists of a generator connected directly to the electrical grid. This system has until recently been dominating completely. The speed of the turbine is determined by the electrical grid frequency, the number of pole pairs of the generator, the slip of the machine and the ratio of the gearbox. A change in wind speed will not affect the speed of the turbine to a large extent, but it will alter the mechanical torque on the shaft, which has effects on the electromagnetic torque and hence, also on the electrical output power. In this way, electric power pulsations will be produced by this type of turbine to a higher extent than by a variable speed turbine. The consequence of the mechanical pulsations, is mechanical stress on the drive train, especially on the gearbox, which is a very expen-

sive component and has a tendency to break down quite often. This turbine type is however rather cheap and robust. In Fig. 2.1 a schematic picture of the fixed speed generator system is shown.

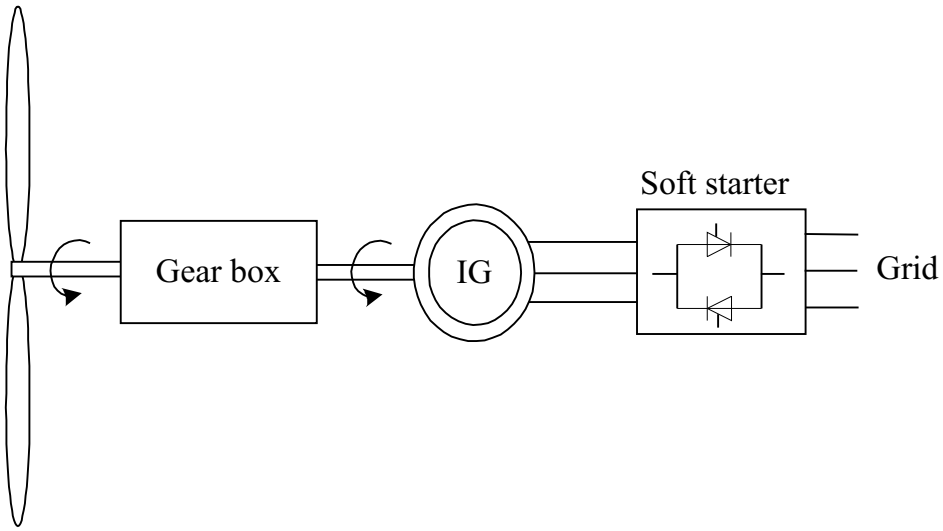

Figure 2.1: The figure show a fixed-speed generator system with the gear box, the short circuited induction generator and a soft starter.

The system either uses two generators or a doubly wounded machine (doubly-wounded means two separate stator windings). At lower wind speeds, a generator with a lower rating and higher number of pole pairs (higher number of pole-pairs means lower rotor speed) is used, which gives aero-dynamic as well as electric loss gainings. In fact it is showed in [1], that this is the most energy efficient turbine available on the market, based on a given blade profile, rotor diameter and maximum mean shaft torque.

2.1.2 Variable Speed System

The variable-speed wind turbine systems are today (2004) continuously increasing their market share. The system utilizes the possibility to store the varying incoming wind power as rotational energy, by changing the speed of the wind turbine. In this way the stress on the mechanical structure is reduced, which also leads to that the electrical power output becomes smoother. The two variable speed systems, the doubly-fed induction generator system (DFIG) and the stator-fed generator system (SFGS), thus have a great degree of freedom in controlling the turbine as well as the grid current. As long as the current levels in the machine or the converter are not violated, reactive power can either be produced or consumed. The generator of the SFGS can either be a conventional synchronous generator (EMSM - Electrically Magnetized Synchronous Machine), a permanent magnet synchronous generator (PMSM) or a conventional induction generator. In case of a multi-pole design there is no need for a gearbox and the

problem with expensive gearbox breakdowns is eliminated. In Fig. 2.2 an illustration of the SFGS multi-pole design is presented, where it can be noted that no gearbox is used.

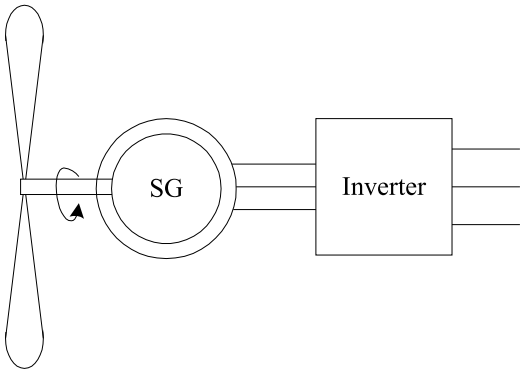

Figure 2.2: Variable-speed multi-pole synchronous generator system, where there is no need for a gearbox.

The DFIG variable speed system utilizes a converter connected, via slip rings, to the rotor circuit of a wounded-rotor induction generator. This system also give a great degree of freedom in controlling the turbine and the grid current, but have one additional advantage, the system only needs a converter that can handle 30% of the rated power of the generator, which imply less losses in addition to the cost reduction [1]. This type of wind energy conversion systems was the most commonly used system produced by the wind turbine manufacturers 2004. In Fig. 2.3 a DFIG-system is presented.

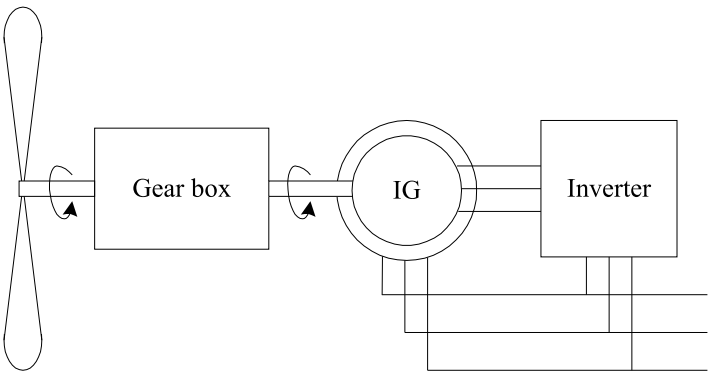

Figure 2.3: Variable-speed doubly-fed induction generator system, where the inverter i connected to the rotor windings.

2.1.3 Aerodynamic Power Control

Stall regulation

The fixed speed system uses an aerodynamical power control method, based on the design of the rotor blades, to limit the upper power level. The method is called stall

regulation and imply that the power is limited at high wind speeds due to that turbulence occur at the lee side of the wind turbine blades and thereby limiting the maximum power to a desired level. The disadvantage is the peak average power that occur at wind speeds around rated wind speed and the power level at the highest wind speeds. This phenomenon is presented in Fig. 2.4, where the effect of different blade angles is shown. In the figure 1 p.u. corresponds to 200kW. It is evident that a great deal of power is lost at higher wind speeds if a blade angle is chosen to limit the maximum power to the rated power at rated wind speed. This can be compensated for, by changing the angle of attack with respect to the wind, at the expense of a even higher power production around rated wind speed. The figure shows different power out-put characteristics at the angles, 0, 1, 3, 5, 7, 9, 11 and 25 degrees for a 180kW wind turbine.

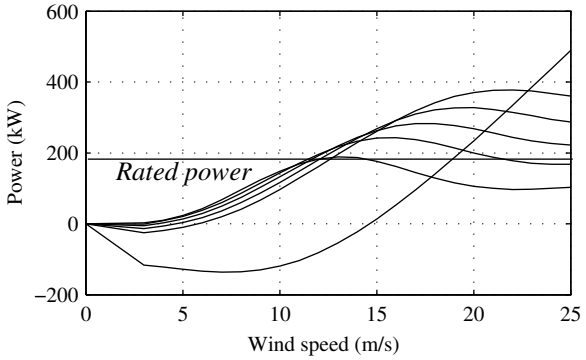

Figure 2.4: The output power of a wind generator system equipped with stall regulation at different pitch angles, where the lowest curve represents 25 degrees and the top one represents 0 degrees.

Active stall control

Multi MW fixed-speed wind turbines use active stall control, which in principle is the same as pitch control. The difference is that the blades are only slightly pitched in order to adjust the power level. The objectives are, in the very low wind-speed region, to pitch the blades in order to control the starting torque and in the high wind speed region, where the power of a conventional stall-regulated wind turbine would either over-shoot or produce to low power, to pitch the blades in order to obtain the rated output power. It is also possible to slightly adjust the pitching angle within the low wind speed areas to optimize the capture of the wind. In addition to the advantageous power control, also for this system the blades can be used as brakes.

Pitch control

In contrary to the fixed speed system, the variable systems use an active aerodynamic power control method. In Fig. 2.5 the wind-speed/power characteristics is shown for

such a system. This method imply that the power is controlled by pitching (turning) the wind turbine blades at higher wind speeds. By pitching the wind turbine blades, the output power can be limited to a desired maximum value at rated wind speeds and above. The drawback of such a system is the pitching mechanism, which leads to additional costs. However, the increased cost due to the pitching mechanism is compensated by the fact that the blades can be used as brakes. Instead of having a large break on the primary side of the shaft, a small one can be used due to the turnable blades.

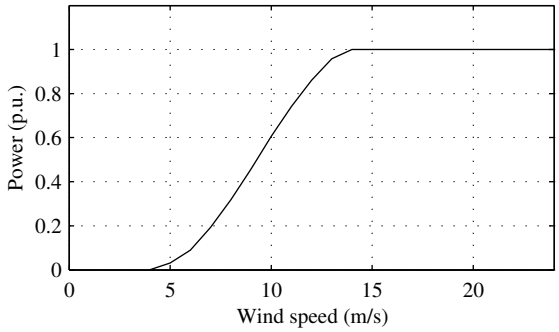

Figure 2.5: The output power of a wind turbine equipped with pitch-control.

2.1.4 Fault Current Contribution

The integration of wind farms into the electrical distribution network is associated with different problems. Earlier, voltage variations (flicker) and harmonics were the main issues, but nowadays utilities and the transmission system operators (TSO's) are mainly interested in the response of wind turbine due to network disturbances. With respect to the power balance in the electrical grid, it is of great importance to maintain power production as long as possible. The contribution of fault current depends on the type of wind turbines used. This has to be taken into consideration in the mechanical dimensioning of the substations and in the protection system configuration of the electrical network with respect to the settings.

Many of the installed wind turbines are fixed speed wind turbines, where the generators are conventional short-circuited induction generators, which contribute to the initial fault current. The peak fault current occurs after 10ms and can be very high. The fault current contribution then continues until the generator is de-magnetized or disconnected from the grid.

The ratio between the number of directly connected generator systems and the number of DFIG systems is changing and as been mentioned before the share of DFIG systems is increasing. The DFIG system has a more controllable fault response, at least for minor disturbances. However, the DFIG turbine installed today have a substantial fault current contribution for larger disturbances and they need approximately 40ms

to disconnect from the grid once a large disturbance occur. So for the mechanical dimensioning of substations, the fault current prediction is still of importance for these systems.

The DFIG system uses a crow-bar to short circuit the the rotor circuit immediately when a large network disturbance occur in order to protect the rotor windings against over voltage, implying that the generator in principle is a short-circuited induction generator during the 40ms, and will therefore behave in a similar manner as directly connected squirrel-cage induction generator. An important point in this discussion is that the DFIG-system may operate at super synchronous or sub-synchronous speed at the time instant of the crow-bar operation. The turbine will therefor slow down or accelerate in order to reach the torque-speed characteristic of the "short-circuited" induction generator if the crow-bar action is initiated. In Fig. 2.6 to Fig. 2.9 the active and reactive power at a crow-bar operation during a low and a high wind speed case are presented. As can be noted the DFIG-system produces/consumes a lot of active and reactive power during the 40ms it takes for the circuit breaker to disconnect the machine.

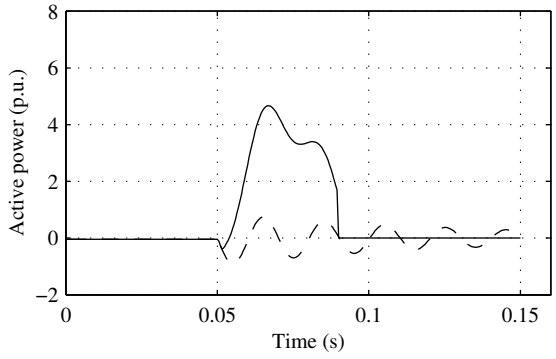

Figure 2.6: The picture show the active effect for a DFIG-system (solid) and for a fixed speed system (dashed) during a 80% voltage dip and when the crow-bar operates, at low wind speed operation.

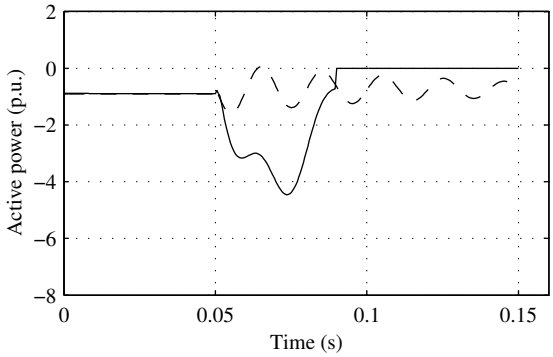

Figure 2.7: The picture show the active effect for a DFIG-system (solid) and for a fixed speed system (dashed) during a 80% voltage dip and when the crow-bar operates, at high wind speed operation.

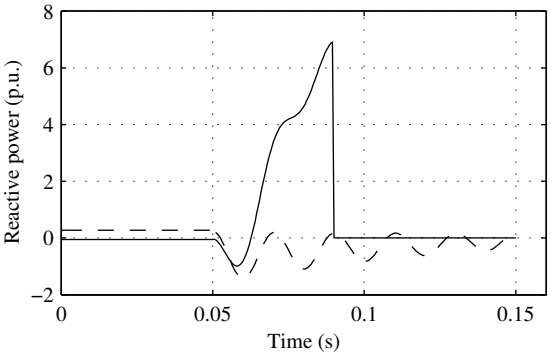

Figure 2.8: The picture show the reactive effect for a DFIG-system (solid) and for a fixed speed system (dashed) during a 80% voltage dip and when the crow-bar operates, at low wind speed operation.

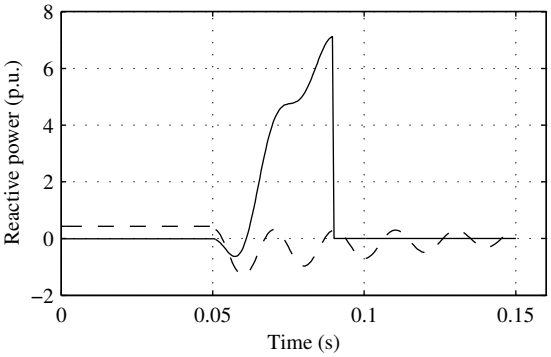

Figure 2.9: The picture show the reactive effect for a DFIG-system (solid) and for a fixed speed system (dashed) during a 80% voltage dip and when the crow-bar operates, at high wind speed operation.

From the figures it is obvious why the DFIG wind turbine must be disconnected

from the grid, once a crow-bar action is initiated.

If the grid disturbances are minor and the voltage and current limitations of the rotor winding and converter are not violated, the system can control the response and the crow-bar does not go into operation. [1].

The variable speed SFGS, where a power converter is mounted between the generator stator and the grid, has a great flexibility in the way it can be set to respond to grid disturbances. Usually the converter is disconnected almost immediately by blocking the pulses to the converter, and accordingly, the fault current contribution can be considered to be negligible.

Chapter 3

Protection Aspects

Distribution networks have originally been designed to transport energy form a high voltage level to a low voltage level and not to accommodate for a significant amount of dispersed generation [5]. The aim to produce approximately 10 TWh of wind energy in about 10-15 years (in Sweden), will however most certainly lead to a change towards more distributed generation.

A large amount of wind power will affect the power flow, the fault currents and the settings of existing protections in the utility grid. This section focuses on the integration of wind power with respect to fault currents and the protective system of the wind turbine.

The protective system configuration is on one hand dependent on the wind turbine manufacturers, and on the other hand on the utilities, who are responsible for the operation of grid. The protective system which is implemented in the wind turbine control system by the manufacturers, protects the wind turbine generator, but must, or at least should, also meet the demands of the utilities and the specified EMC-levels. EMC stands for Electromagnetic Compatibility and is a state at which electrical equipment works satisfactorily in the electromagnetic environment without interfering with other equipment. The EMC-level gives a certain threshold value for which EMC is expected, e.g., the voltage level should be held within 207 - 244 V [23].

3.1 Specification of Protections and Settings

Three different categories of protection related to wind turbines and the connection of wind turbines can be identified (A, B and C). The three categories are compared in the following sections with respect to the protection settings.

3.1.1 Protection in Accordance with the Swedish Regulations for Establishments (A)

The categories of protection for wind turbines in Sweden, are specified in *Swedish regulations for establishments*, which are associated with high current levels that could cause injury or damage to people, animals or property [24]. The regulations specify that protection should be provided for; over-current (over load and short circuit), earth-fault, over-voltage and under-voltage. However, the regulations do not provide any information about settings, but recommend that any situation unsafe for people, animals or property should be eliminated as quickly as possible.

3.1.2 Protection of the Wind Turbine (B)

The wind turbine protection system shall protect the wind turbine from external faults, i.e. faults on the utility grid. According to the protection scheme for a 600kW wind turbine from a known wind turbine manufacturer, the protective system includes:

- Over current protection, i.e. over-load protection and short-circuit protection.
- Over- and under-voltage protection
- Surge arrester
- Over- and under-frequency protection
- Reversed-power protection

In the technical specifications for the 600 kW wind turbine, the over- and the under voltage protection as well as the frequency protection has the following settings, see Table 3.1

Table 3.1: Settings for voltage and frequency protection for a 600 kW wind turbine.

Protection	High/Low	Levels	Time settings
Voltage	High 1	424 V	60 s
	Low 1	360 V	60 s
	High 2	434 V	0.3 s
	Low 2	337 V	0.5 s
Frequency	High	50.5 Hz	0.2 s
	Low	49.5 Hz	0.2 s

3.1.3 Protection of the Utility Grid - AMP Regulations (C)

In [25] recommendations of protections for wind turbines is presented. The report specifies the different protections that the utilities probably will demand, for the electrical grid to have adequate protection against faults in the wind turbine. The instructions concern smaller wind turbines - max. 1500kW. However, the instructions are valid also for wind farms, since it is the power of a separate wind turbine that sets the standard. The AMP (Anslutning av Mindre Produktionsanläggningar till Elnätet) is summarized below, with respect to the protection requirements.

- Three phase over- and under voltage protection. Slow voltage variations +6%, -10%, disconnection within 10 seconds, ±20% disconnection within 0.2 seconds.
- Reversed power protection. If the generator runs as a motor, disconnection within 5 seconds.
- Short circuit protection. Fuses or circuit breakers, depending on the size of the generator or/and the grid impedance.
- Protection against island operation

If the generator is equipped with reactive power compensation, exceeding the reactive power consumption in no load operation, there is a risk for self-magnetization of the induction generator in case that the turbine and the local grid is disconnected from the main electrical grid. If the capacitors is not disconnected or controlled within 0.1 seconds, the generator shall be protected against uncontrolled island operation, which shall disconnect the generator within 0.2 seconds. The protection may consist of voltage- and frequency protection.

It is recommended that the generator system is equipped with earth fault protection, which disconnects the generator if there is an earth fault in the distribution network. If only over- and under voltage protection together with over- and under frequency protection are used, earth faults are detected by a *NUS*, (Nätunderspänningsskydd), which is placed on the secondary side of the step-up transformer in case the neutral point of the transformer primary (high-voltage) side is not connected, see Fig. 3.1.

The grid under-voltage protection should operate if the voltage drop is between 20 - 30%. Over-voltage protection and frequency protection are used as a redundancy if self-magnetizing occurs. Over voltage protection should disconnect the generator if the voltage exceeds the rated value by 20% and frequency protection disconnects the generator as quickly as possible if the frequency falls below 47 Hz or exceeds 51 Hz.

The protection settings according to category B and C, are sometimes contradictory, but should be identical. Due to this uncertainty, the utilities sometimes demand external protections, which imply additional costs. Different opinions of the wind turbine manufacturers/wind turbine owners, who are interested in protecting the wind

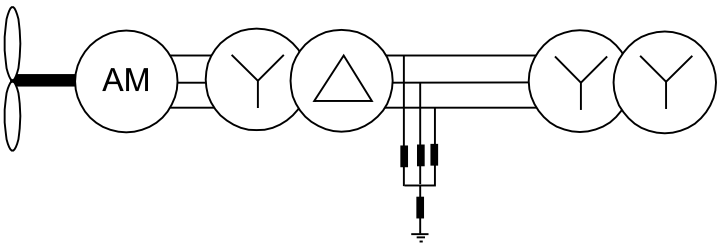

Figure 3.1: The incorporation of a *NUS*

turbine and maintaining power production as far as possible, and the utilities, who are interested in protecting the grid, may arise. Especially today, where there is a demand from the TSO's that wind turbines should disconnect themselves only when it is absolutely necessary. The differences in voltage and frequency settings can be seen by comparing Table 3.1 and the recommendations according to AMP and are presented in Table 3.2.

Desirable would be if the settings according to B and C were in accordance with each other. Most of the utilities and the entrepreneurs are following AMP and as the protection settings of the wind turbines differs, this could cause problems. An investigation at Gotland showed that 12 out of 16 wind turbines did not fulfil the demands on the settings for the protective systems [10]. The Gotland utility nowadays demand the possibility to test and change the settings of the wind turbine protection system. In view of this fact it is not difficult to see why external protections sometimes are demanded.

Table 3.2: Different settings according to protection category B and C.

Protection category		B	C		B	C
Voltage setting	High 1	+6%	+6%	High 2	+8.5%	+20%
Time setting	High 1	60 s	10 s	High 2	0.3 s	0.2 s
Voltage setting	Low 1	−10%	−10%	Low 2	−16%	−20%
Time setting	Low 1	60 s	10 s	Low 2	0.5 s	0.2 s
Frequency setting	High	50.5 Hz	51 Hz			
Time Setting	High	0.2 s	0.2 s			
Frequency setting	Low	49.5 Hz	47 Hz			
Time setting	Low	0.2 s	0.2 s			

In England and France, utilities responsible for the operation of the electrical grid demand to have full control of the protective equipment and its operating functions, which is why they demand external protective equipment. As mentioned earlier, this is becoming a standard procedure even in Sweden and the additional equipment of course leads to increased installation costs.

3.2 Coming Demand on Wind Turbine Immunity Levels

As the amount of wind power increases the need for accurate protective systems increase. The significance of the wind energy production is no longer negligible and disconnection of large groups of wind turbines can not be accepted, unless it is absolutely necessary. A massive disconnection of wind power production may lead to a power system collapse. This has lead to that utilities and TSO's have started to put up regulations for when a wind turbine is allowed to be disconnected.

In Sweden, demands on larger wind turbine installations to withstand a reference voltage dip has been proposed by Svenska Kraftnät. The proposed voltage dip is presented in Fig. 3.2.

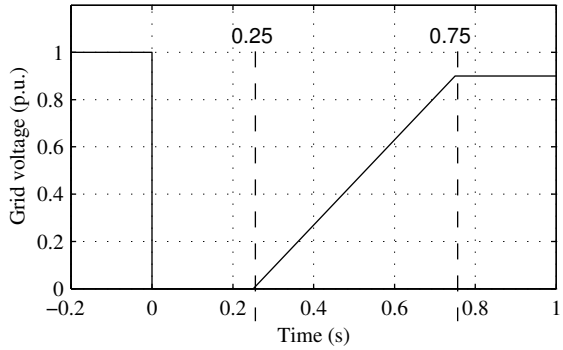

Figure 3.2: Reference voltage dip for larger wind turbine installations.

From Fig. 3.2 it can be noted that the wind turbine installation shall withstand a 100% voltage dip during 250 ms, then rising to 90% of the nominal grid voltage during the next 500 ms. For any less severe voltage dips the wind turbine must stay connected to the grid.

Chapter 4

Short Circuit Calculations, IEC 909

Currents due to electrical faults can have a very high magnitude, compared to the currents at normal operation. In this section, the IEC 909 standard, for short circuit calculations is presented. The calculations are made for three phase short circuit faults, since a three-phase fault represent the worst case scenario and is mechanically dimensioning of e.g. substations. The IEC 909 standard also provides methods to calculate the steady state short-circuit current, but since severe faults and the transient behavior of the induction machine are the objectives, the following chapter will focus on calculating the peak short-circuit current.

4.1 Short Circuit Currents in a Three-Phase AC Grid

AC networks can be represented, according to Thevenin's theorem, by a voltage source and an impedance. The voltage corresponds to the voltage before a fault occurs (normally the nominal voltage)and the impedance is represented by a resistance and an inductance. In reality, the AC network also contains line capacitances, but they are of little significance in short circuit calculations and are usually neglected [9]. The circuit presented in Fig. 4.1 is a sufficient representation of the electrical grid for short circuit calculations.

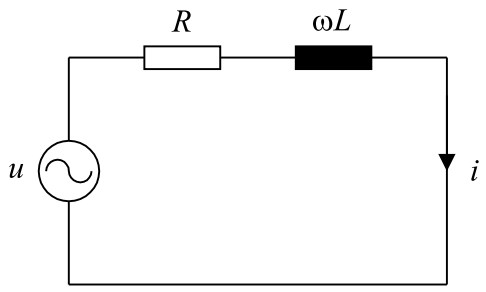

Figure 4.1: Electrical grid representation for short circuit calculations

There are also a few more basic assumptions made in order to simplify the short circuit calculation procedure. Theses assumptions are

- The impedance of the short circuit is assumed to be zero.
- Load currents are neglected.
- Nominal values of voltages are assumed.
- Motors are assumed to be working at rated power.
- If the R/X ratio is unknown, a low value is assumed, since this will give a high peak current factor.
- The impedance of the busbars in the switch gears are neglected.

It is however recommended that, any of these assumptions are eliminated and replaced with more accurate values if possible.

Suppose that a short circuit occurs at $t = 0$, and that the voltage varies according to

$$u = \hat{u}\sin(\omega t + \alpha) \tag{4.1}$$

where α is an arbitrary angle, representing the voltage phase angle at the time instant of the short circuit. According to Kirchoff's voltage law, the circuit equation can be written as,

$$L\frac{di_{sc}(t)}{dt} + Ri_{sc}(t) = \hat{u}\sin(\omega t + \alpha) \tag{4.2}$$

which has the solution

$$i_{sc}(t) = i_{dc}(t) + i_{ac}(t) \tag{4.3}$$

where i_{ac} is the stationary alternative short circuit current, leading the voltage by an angle φ and i_{dc} is a direct current component, decaying exponentially with time. The AC component can be written according to

$$i_{ac}(t) = \frac{\hat{u}}{\sqrt{(\omega L)^2 + R^2}}\sin(\omega t + \alpha - \varphi) \tag{4.4}$$

where

$$\varphi = \arctan \frac{\omega L}{R} \tag{4.5}$$

and

$$\sqrt{(\omega L)^2 + R^2} = |Z| \tag{4.6}$$

The exponentially decaying direct current component can be written according to

$$i_{dc}(t) = Ae^{-\frac{t}{T}} \tag{4.7}$$

where $T = L/R$. Hence, the total short circuit current can be expressed as

$$i_{sc}(t) = i_{ac}(t) + i_{dc}(t) = \frac{\hat{u}}{\sqrt{(\omega L)^2 + R^2}} \sin(\omega t + \alpha - \varphi) + Ae^{-\frac{t}{T}} \tag{4.8}$$

The constant A is determined by the conditions that, $i_{sc}(t) = 0$ at $t = 0$. Inserting this in (4.8), the equation can be rewritten as

$$A = -\frac{\hat{u}}{\sqrt{(\omega L)^2 + R^2}} \sin(\alpha - \varphi) \tag{4.9}$$

and the complete solution can be expressed as

$$i_{sc}(t) = \frac{\hat{u}}{\sqrt{(\omega L)^2 + R^2}} [\sin(\omega + \alpha - \varphi) - e^{-\frac{t}{T}} \sin(\alpha - \varphi)] \tag{4.10}$$

Further, (4.10) can be rewritten as

$$i_{sc}(t) = \sqrt{2} I''_{sc} [\sin(\omega + \alpha - \varphi) - e^{-\frac{t}{T}} \sin(\alpha - \varphi)] \tag{4.11}$$

where the initial short circuit current, i''_{sc}, is defined as the RMS value of the a.c. symmetrical component of a prospective short circuit current (prospective short circuit current means the current that would flow if the short circuit were replaced by an ideal connection of negligible impedance without any change in supply).

$$I''_{sc} = \frac{\hat{u}}{\sqrt{2}|Z|} \tag{4.12}$$

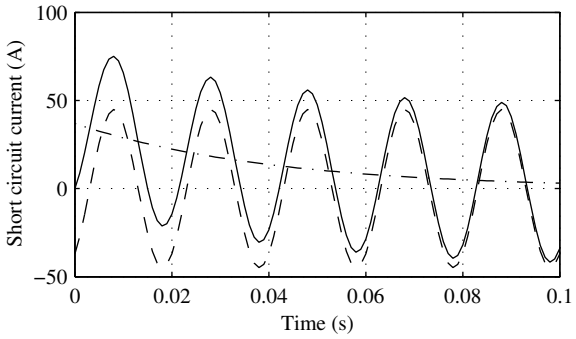

Figure 4.2: The components originated from a short circuit.

In Fig. 4.2, the different components which originate from a short circuit are shown. The peak short circuit current is the sum of the AC and the DC component at 10 ms after the instant of the short circuit and represents the highest value of the short circuit current.

The peak current is mechanically dimensioning of e.g. substations and can be calculated according to

$$I_p = \kappa\sqrt{2}I''_{sc} \tag{4.13}$$

where κ is the peak current factor and represents the relationship between the peak current and the peak value of the stationary short circuit current, $i_{ac}(t)$. The value of the peak current varies with the angle α, i.e. the voltage phase angle at the time instant of the short circuit and the ratio, R/X. The peak current factor can be calculated according to

$$\kappa = 1,02 + 0,98e^{-3\frac{R}{X}} \tag{4.14}$$

4.2 Short-Circuit Current Calculations for the Induction Machine

When the initial symmetrical short circuit current is calculated, the absolute value of the induction machine's locked rotor impedance, Z_{LR} is used. Z_{LR} represents the impedance of the induction machine corresponding to the highest symmetrical RMS current of an induction machine with a locked rotor, and fed with rated voltage at rated frequency. Since the sub-transient impedance is not always stated by the manufacturer, the locked rotor impedance is often used, which can be calculated according to

$$Z_{LR} = \frac{1}{I_{LR}/I_n} \cdot \frac{U_n}{\sqrt{3}I_n} \tag{4.15}$$

where I_{LR} is the locked rotor current at rated voltage. I_n and U_n is the rated current and the rated voltage of the machine.

The initial short circuit current, which corresponds to the RMS value of the AC component of the short circuit current in (4.10), is calculated according to

$$I''_{sc} = \frac{cU_n}{\sqrt{3}Z_{LR}} \tag{4.16}$$

where U_n is the nominal voltage of the network and c is a voltage factor. The value of c depends on many factors, for example operational voltage of cables or overhead lines and location of short circuit. In Table 4.1 the specified values are presented.

Table 4.1: Voltage factor c

Nominal voltage	Max. short circuit current c_{max}
Low voltage (100V-1kV)	1.00 (230V/400V) 1.05 (other voltages)
Medium voltage (>1kV-35kV)	1,10
High voltage (>35kV-230kV)	1,10

Note: cU_n should not exceed the highest value for equipment in the power system.

Finally, the peak short circuit current can be calculated according to (4.13).

The operational data of the 15 kW squirrel-cage induction machine, used for measurement in the thesis, are presented in table 4.2

Table 4.2: The data plate information of the 15 kW induction machine

U_n	$380V$
I_n	32
P_n	15 kW
$\cos\phi$	0,81
n	970 r/min
f	50 Hz

An unknown parameter in this case is however I_{LR}, which can be found in a more detailed data sheet that sometimes can be provided by the manufacturer. Such a detailed data sheet was available for the 15 kW machine and the ratio L_{LR}/I_n was found to be 6,81.

Performing the calculations according to (4.15) and (4.16), using the values according to the data plate, will in the end provide us with an estimate of the initial short circuit current. The peak value of the current is according to (4.13) dependent on the peak current factor, κ and according to (4.14) this factor is dependent on the R/X ratio of the induction machine. The manufacturer data sheet provides us with the information of interest, $R = 0,37\Omega$ and $X = 1,42\Omega$ (The parameters in this case can be derived using the information in table 6.1).

The κ can now be calculated according to (4.14)

$$\kappa = 1,02 + 0,98e^{-3\frac{R}{X}} = 1,47 \tag{4.17}$$

The locked rotor impedance is calculated according to (4.15)

$$Z_{LR} = \frac{1}{6,81} \cdot \frac{380}{\sqrt{3}I_n} = 1,01\Omega \tag{4.18}$$

and the initial short circuit current according to

$$I_{sc}^{''} = \frac{380}{\sqrt{3} \cdot 1,01} = 217A \tag{4.19}$$

where the voltage factor, c, has been set to one. I_p can finally be determined according to (4.14)

$$I_p = \kappa\sqrt{2}I_{sc}^{''} = 1,48 \cdot \sqrt{2} \cdot 217 = 451A \tag{4.20}$$

This result will be compared with the three-phase short circuit measurements of the squirrel-cage induction machine in chapter 5.

Chapter 5

Induction Machine Modelling

In this section the fundamental theory behind dynamic modelling of the induction machine is presented. The concept of using space vectors, associated with the conventional induction machines models is presented. Furthermore, a detailed two axis model and a three-phase model, for analysis of symmetrical and asymmetrical fault conditions respectively are derived. Both models take the skin effect and the saturation of the leakage-flux paths into consideration.

5.1 Space Vectors

The three phase windings of the stator in a three phase induction machine, as voltage is applied, carries a current which will cause a magnetic flux to appear. The related current vector is parallel with the magnetic axis of one phase. Each phase current can be represented by a current vector and if the three instantaneous current vectors are added vectorially, a resultant current vector is formed, $\vec{i}_{res}$, see Fig. 5.1.

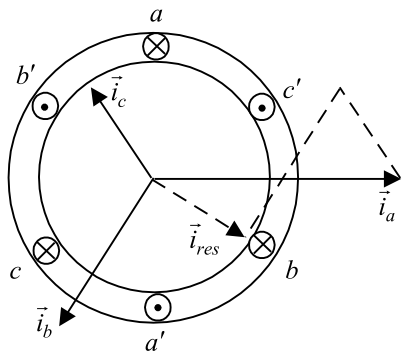

Figure 5.1: Current vector representation.

The mathematical expression of this current vector is

$$\vec{i}_{res} = 2/3(i_a + ai_b + a^2 i_c) \tag{5.1}$$

where the operator a is equal to $e^{j2\pi/3}$.

In a three phase induction machine, the three windings interact with each other. The flux created by the current in one of the phase windings affects the other two windings in such a way that, the resultant flux, affecting each one of the three phase windings, is 3/2 times the flux created by the current running through the phase winding itself. Hence, multiplying the resultant current vector by 2/3 give us the phase current magnitude. This will be treated further later in this section.

The conventional model of the induction machine described by space vectors are associated with a few simplifications:

- The distribution of the flux linkage wave is sinusoidal
- The magnetization characteristic of the machine is linear
- The iron losses are neglected
- The leakage inductances and resistances are independent of temperature, frequency and current.

5.1.1 Voltage, Current and Flux

The stator voltages of a three-phase induction machine can be described by the following voltage equations

$$u_{sa} = R_s i_{sa} + \frac{d\psi_{sa}}{dt} \tag{5.2}$$

$$u_{sb} = R_s i_{sb} + \frac{d\psi_{sb}}{dt} \tag{5.3}$$

$$u_{sc} = R_s i_{sc} + \frac{d\psi_{sc}}{dt}. \tag{5.4}$$

where R_s is the stator resistance, u_s the stator voltage, i_s the stator and ψ_s the stator flux. Due to the given physical orientation of the windings in the machine (120° apart), quantities such as flux and voltage can be expressed by means of space vectors,

$$\vec{u}_s = \frac{2}{3}K\big(u_{sa} + u_{sb}e^{j2\pi/3} + u_{sc}e^{j4\pi/3}\big) \tag{5.5}$$

$$\vec{\psi}_s = \frac{2}{3}K\big(\psi_{sa} + \psi_{sb}e^{j2\pi/3} + \psi_{sc}e^{j4\pi/3}\big). \tag{5.6}$$

The factor K in (5.5) and (5.6) can vary depending on if a peak-value scaling, a RMS-value scaling or if a power invariant scaling is desired. K equal to 1 corresponds to a peak value scaling, i.e. the magnitude of the space vector has the same magnitude as the peak value of the phase quantities, which can be an advantage since phase

quantities often are used. If a RMS-value scaling is desired K is chosen as $1/\sqrt{2}$ and if a power invariant scaling is to be used, the factor K is chosen to be $\sqrt{3/2}$. In this work, a peak value scaling has been chosen, i.e. $K = 1$.

using complex notation, (5.5) can be expressed as

$$\vec{u}_s = R_s\vec{i}_s + \frac{d\vec{\psi}_s}{dt} \tag{5.7}$$

which can be separated into a real and a imaginary part, i.e. a two axis representation, Fig. 5.2.

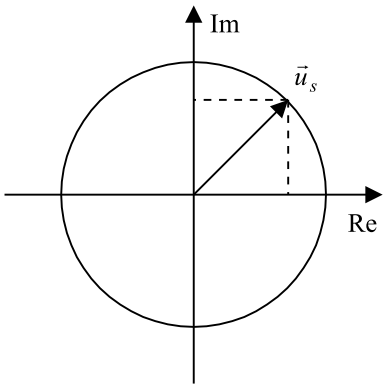

Figure 5.2: Two axis representation of a voltage vector.

The stator-voltage equation (5.7) is referred to the stator frame, i.e. a stationary reference frame. This reference frame is referred to as the $\alpha\beta$-system, where α represents the real axis and β the imaginary axis. A common form to express the transformation from a three phase system into a two axis system is in matrix-form, where the elements in the transformation matrix can be identified from (5.5), if the equation is written on rectangular form $(x + jb)$.

$$\mathbf{U} = \begin{bmatrix} u_\alpha \\ u_\beta \\ u_0 \end{bmatrix} = \frac{2}{3}\begin{bmatrix} 1 & -\frac{1}{2} & -\frac{1}{2} \\ 0 & \frac{\sqrt{3}}{2} & -\frac{\sqrt{3}}{2} \\ 1/2 & 1/2 & 1/2 \end{bmatrix} \times \begin{bmatrix} u_{sa} \\ u_{sb} \\ u_{sc} \end{bmatrix}$$

For a two-axis model it is an advantage to refer all equations to the same reference frame, also the rotor quantities. For a specific purpose, the stator reference frame may be the most suitable, but in an other case a rotating reference frame is preferable. Fig. 5.3 show a stationary reference frame (s) and an arbitrary rotating reference frame (k) in the same coordinate system, and the following equations show how to transform, for instance a voltage vector, from one reference frame to another.

The voltage vector in a stationary reference frame can be defined by a magnitude and a phase angle δ.

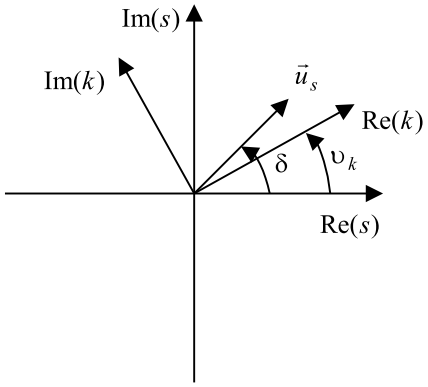

Figure 5.3: Stationary (s) and a arbitrary (k) reference frame in the same coordinate system.

$$\vec{u}^s = \hat{u}e^{j\delta} \tag{5.8}$$

The voltage vector referred to an arbitrary reference frame can be expressed as

$$\vec{u}^k = \hat{u}e^{j(\delta-\nu_k)} = \vec{u}^s e^{-j\nu_k} \tag{5.9}$$

which gives

$$\vec{u}^s = \vec{u}^k e^{j\nu_k}. \tag{5.10}$$

If the stator voltage according to (5.7) is transformed to an arbitrary reference frame, the voltage vector can be written according to (5.10)

$$\vec{u}_s^s = \vec{u}_s^k e^{j\nu_k}. \tag{5.11}$$

In the same way, the flux and the current can be written as

$$\vec{\psi}_s^s = \vec{\psi}_s^k e^{j\nu_k} \tag{5.12}$$

$$\vec{i}_s^s = \vec{i}_s^k e^{j\nu_k}. \tag{5.13}$$

Inserting the voltage, flux and current expressed in the arbitrary reference frame into (5.7), yields

$$\vec{u}_s^k e^{j\nu_k} = R_s \vec{i}_s^k e^{j\nu_k} + \frac{d(\vec{\psi}_s^k e^{j\nu_k})}{dt} \tag{5.14}$$

which by performing the derivation of the product $(\vec{\psi}_s^k e^{j\nu_k})$ can be written as

$$\vec{u}_s^k e^{j\nu_k} = R_s \vec{i}_s^k e^{j\nu_k} + \frac{d\vec{\psi}_s^k}{dt} e^{j\nu_k} + j\frac{d\nu_k}{dt}\vec{\psi}_s^k e^{j\nu_k}. \tag{5.15}$$

The term $d\nu_k/dt$ is the same as the angular velocity of the rotating reference frame, ω_k and the term $e^{j\nu_k}$ can be eliminated. The final expression of the complex voltage equation can be expressed according to

$$\vec{u}_s^k = R_s\vec{i}_s^k + \frac{d\vec{\psi}_s^k}{dt} + j\omega_k\vec{\psi}_s^k. \tag{5.16}$$

In the same way, the rotor equation for an arbitrary rotating reference frame can be derived. The rotor equation can accordingly be expressed as

$$\vec{u}_r^k = R_r\vec{i}_r^k + \frac{d\vec{\psi}_r^k}{dt} + j(\omega_k - \omega_r)\vec{\psi}_r^k \tag{5.17}$$

where the angular velocity, ω multiplied by the flux linkage, ψ corresponds to the back emf (electro-motive force). R_r is the rotor resistance and U_r the rotor voltage.

5.1.2 Instantaneous Power and Torque

The active and the reactive power of any electrical circuit are defined as [11]

$$P = Re[\vec{u}_s^k(\vec{i}_s^k)^*] \tag{5.18}$$
$$Q = Im[\vec{u}_s^k(\vec{i}_s^k)^*] \tag{5.19}$$

If the expressions for the voltage vectors and the current vectors are introduced, this yields

$$S = [\vec{u}_s^k(\vec{i}_s^k)^*] = \big(\frac{2K}{3}\big)^2)(u_a + au_b + a^2u_c)(i_a + ai_b + a^2i_c)^* \tag{5.20}$$

where $a = e^{j2\pi/3}$. As $a^2 = e^{j4\pi/3}$ is equal to $e^{-j2\pi/3}$, the expression can be written according to

$$S = \big(\frac{2K}{3}\big)^2(u_a + u_be^{j2\pi/3} + u_ce^{-j2\pi/3})(i_a + i_be^{-j2\pi/3} + i_ce^{j2\pi/3}) \tag{5.21}$$

Further, rewriting of the expression yields

$$\begin{aligned}
S &= \big(\frac{2K}{3}\big)^2(u_ai_a + u_ai_be^{-j2\pi/3} + u_ai_ce^{j2\pi/3} + u_bi_ae^{j2\pi/3} + u_bi_b + u_bi_ce^{-j2\pi/3} \\
&+ u_ci_ae^{-j2\pi/3} + u_ci_be^{2\pi/3} + u_ci_c) = \\
&\big(\frac{2K}{3}\big)^2(u_ai_a + u_bi_b + u_ci_c + (u_ai_b + u_bi_c + u_ci_b)e^{-j2\pi/3} \\
&+ (u_ai_c + u_bi_a + u_ci_b)e^{j2\pi/3}) = \\
&\big(\frac{2K}{3}\big)^2(u_ai_a + u_bi_b + u_ci_c + (u_ai_c + u_bi_a + u_ci_b)e^{j2\pi/3} \\
&- (u_a(i_a + i_c) + u_b(i_b + i_a) + u_c(i_b + i_c))e^{-j2\pi/3}) = \\
&\big(\frac{2K}{3}\big)^2[\frac{3}{2}(u_ai_a + u_bi_b + u_ci_c) + j\frac{\sqrt{3}}{2}(u_a(i_c - i_b) + u_b(i_a - i_c) + u_c(i_b - i_a))]
\end{aligned}$$

According to (5.18) and (5.19) P and Q are defined as

$$P = \big(\frac{2K}{3}\big)^2(u_a i_a + u_b i_b + u_c i_c) \tag{5.22}$$

$$Q = \big(\frac{2K}{3}\big)^2\frac{\sqrt{3}}{2}(u_a(i_c - i_b) + u_b(i_a - i_c) + u_c(i_b - i_a) \tag{5.23}$$

and if a the power is to be calculated the power invariant scaling is chosen, i.e. K equal to $\sqrt{3/2}$, which give us

$$P = (u_a i_a + u_b i_b + u_c i_c) \tag{5.24}$$

$$Q = \frac{1}{\sqrt{3}}(u_a(i_c - i_b) + u_b(i_a - i_c) + u_c(i_b - i_a). \tag{5.25}$$

In a generator, mechanical power is converted to electrical power. Parts of the active electrical power is related to losses in the stator and the rotor resistance and stored magnetic energy in the inductances. The total electrical power from the generator can be expressed as

$$\begin{aligned} P_e &= Re[\vec{u}_s^k(\vec{i}_s^k)^*] = Re[(\vec{i}_s^k R_s + \frac{d\vec{\psi}_s^k}{dt} + j\omega_k\vec{\psi}_s^k)(\vec{i_s^k})^*] \\ &= R_s|\vec{i}_s^k|^2 + Re[(\frac{d\vec{\psi}_s^k}{dt} + j\omega_k\vec{\psi}_s^k)(\vec{i}_s^k)^*] \\ &= R_s|\vec{i}_s^k|^2 + Re[(\frac{d\vec{\psi}_s^k}{dt}(\vec{i}_s^k)^*] + Re[j\omega_k\vec{\psi}_s^k(\vec{i}_s^k)^*]. \end{aligned}$$

From the expression above, one can identify three different parts, related to resistive losses, stored magnetic energy (power) and the mechanical power. The electromechanical power also can be expressed as torque multiplied by a angular displacement, i.e. the angular velocity

$$P_e = T_e\omega_k \tag{5.26}$$

where the electromechanical torque can be identified as

$$T_e = Im[\vec{\psi}_s^k(\vec{i}_s^k)^*]. \tag{5.27}$$

The expression of the electromechanical torque is general, and holds for any of the models described in the following sections. The equation of motion for the induction machine can be expressed according to

$$T_e - T_m = J\frac{d\Omega_m}{dt} \tag{5.28}$$

where T_m is the mechanical torque, Ω_m the mechanical angular speed in mechanical rad/s and J the inertia of the induction machine.

5.2 The Two Axis Model

From the previous section, one can derive the dynamic equivalent circuit of the induction machine. The induction machine consist of the rotor and the stator windings, which is separated by the air gap. The connection between the two sides (the rotor and the stator) is electromagnetic, where iron in the stator and the rotor facilitate the path of the flux and helps strengthen the interconnection between the two windings. Equations (5.16) and (5.17) helps us to identify the different parameters of the induction machine. The first part in (5.16) and (5.17) represents the resistive losses in the stator and the rotor winding and the second part can be written according to

$$\frac{d\vec{\psi}_s^k}{dt} = (L_{s\lambda} + L_m)\frac{d\vec{i}_s^k}{dt} + L_m\frac{d\vec{i}_r^k}{dt} \tag{5.29}$$

$$\frac{d\vec{\psi}_r^k}{dt} = (L_{r\lambda} + L_m)\frac{d\vec{i}_r^k}{dt} + L_m\frac{d\vec{i}_s^k}{dt} \tag{5.30}$$

and are dependent on current changes during the operation of an induction machine. The leakage inductances $L_{s\lambda}$ and $L_{r\lambda}$ are related to the stator and the rotor side respectively, whereas the magnetizing inductance is related to both sides, since both the stator and the rotor are affected by the (main) magnetizing flux. The third part in (5.16) and (5.17) represents the speed voltage or the induced voltage (back emf) in the machine.

The most common way of representing the induction machine is the T-model, also known as the Park-model [17], which is presented in Fig. 5.4.

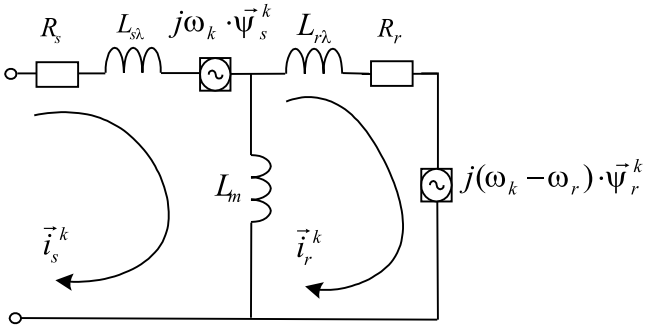

Figure 5.4: The equivalent T-model of the induction machine, also known as the Park-model.

The parameters necessary to describe the induction machine by the fifth-order T-model, can be obtained from the manufacturer, by performing FEM (Finite Element Method) computations [18] or by means of experiments [20]. If the parameters are to be determined by means of measurements, a locked rotor test, a no load test and

measurement of the stator resistance are needed.

The T-model is physically relevant, but it is less good from an analysis and control standpoints of view, since it is over-parameterized [14]. As a consequence there is a difficulty in determining the distribution between the stator and the rotor leakage inductances from measured data. This is reflected by the ways of finding the values of the stator and the rotor leakage inductances, which are assumed to be equally distributed. An other way is to use an empirical splitting factor. In [13] the following distribution, for motors in general, is suggested

$$L_{s\lambda} = \frac{2}{3} L_{r\lambda}. \tag{5.31}$$

The difficulty in determining the parameters of the T-model can be avoided by using the Γ-model presented in Fig. 5.5, where both of the leakage inductances are referred to the rotor side. The Γ-model has been derived by, e.g. [6] and [19] and predicts identical results compared with the T-model. Using this model, the problem with the over-parametrization is eliminated and in the same way as for the T-model, the parameters can be determined from the conventional measurements, i.e. a no-load test and a locked-rotor test together with measurement of the stator resistance.

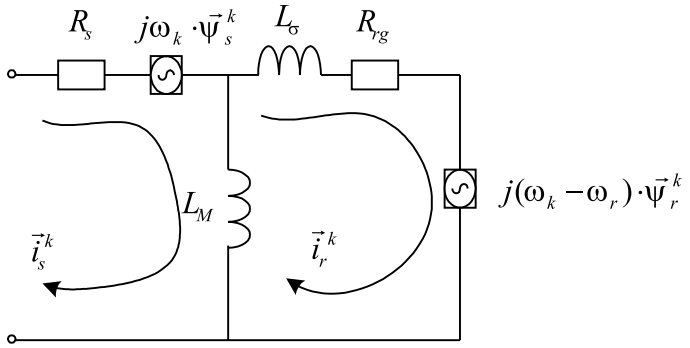

Figure 5.5: A Γ-model representation of the induction machine.

The induction machine parameters for the T-model are usually given by the manufacturer, but the parameters of the Γ-model can easily be calculated by using equation (5.32)-(5.34).

$$R_{rg} = \left(\frac{L_s}{L_m}\right)^2 R_r \tag{5.32}$$

$$L_\sigma = \frac{L_s}{L_m}\left(L_{s\lambda} + \frac{L_s}{L_m} L_{r\lambda}\right) \tag{5.33}$$

$$L_M = L_{s\lambda} + L_m. \tag{5.34}$$

where $L_s = L_{s\lambda} + L_m$.

From measurements, the Γ-model parameters can be determined directly according to (5.35) and (5.36):

$$X_\sigma = \frac{-X_M^2 X_{LR} + X_M X_{LR}^2 + R'^2_{LR} X_M}{2X_{LR}X_M - X_M^2 - X_{LR}^2 - R'^2_{LR}} \tag{5.35}$$

$$R_{rg} = R'_{LR}\frac{X_M + X_\sigma}{X_M - X_{LR}} \tag{5.36}$$

where

$$R'_{LR} = R_{LR} - R_s \tag{5.37}$$

$$X_M = X_{s\lambda} + X_m = X_0 \tag{5.38}$$

$$\tag{5.39}$$

and X_0 is the no-load reactance, R_s is the measured DC resistance of the stator winding and the subscript LR indicates locked rotor parameters.

5.3 A More Detailed Model for Transient Conditions

A starting point for the derivation of a more detailed induction machine model is the fundamental equations of the traditional induction machine model. In this subsection the electrical equations of the Γ-model are presented as well as derivation of the equations for rotation, i.e. the torque equation. The equations are presented for an arbitrary rotating reference frame for the two axis model.

According to the previous section, the equations for the stator and the rotor voltage can be expressed as

$$\vec{u}_s^k = R_s\vec{i}_s^k + \frac{d\vec{\psi}_s^k}{dt} + j\omega_k\vec{\psi}_s^k \tag{5.40}$$

$$\vec{u}_r^k = R_s\vec{i}_r^k + \frac{d\vec{\psi}_r^k}{dt} + j(\omega_k - \omega_r)\vec{\psi}_r^k \tag{5.41}$$

where the stator- and the rotor flux can be written as

$$\vec{\psi}_s^k = L_M\vec{i}_s^k + L_M\vec{i}_r^k \tag{5.42}$$

$$\vec{\psi}_r^k = L_r\vec{i}_r^k + L_M\vec{i}_s^k. \tag{5.43}$$

Further, the rotor inductance L_r is defined as

$$L_r = L_\sigma + L_M \tag{5.44}$$

$$\tag{5.45}$$

where L_σ is the "rotor" leakage inductance and L_M is the magnetizing inductance of the induction machine, both referred to the Γ-model.

5.3.1 Incorporating Skin Effect and Leakage Flux Saturation

The conventional models presented in the previous section are not sufficient to describe the induction machine dynamics when severe disturbances in the voltage supply occur. A more extensive model is needed, i.e. a model taking phenomena, such as skin effect in the rotor conductors and saturation of the leakage flux path into account. In this section it is described how these two important phenomena are incorporated in the induction machine model. There are of course other phenomena which occur at abnormal operating conditions, e.g. increased temperature and saturation of the magnetizing inductance and the magnetizing resistance, L_m and R_m, but the two previous mentioned aspects are the most important when fault current prediction of mains-connected induction machines are the objective.

Implementation of the Skin Effect

Electromagnetic waves are attenuated as it propagates in a conductor. The distance δ at which the amplitude of a travelling plane wave decreases by a factor of e^{-1} or 0.368 is called the *skin depth*. The penetration depth of the magnetic field, into the current carrying conductors is reciprocally proportional to the frequency and can be written as

$$\delta = \frac{1}{\sqrt{\pi f \mu \sigma}} \tag{5.46}$$

where μ is the permeability of the material and σ is the conductivity.

In slip-ringed induction machines, used in DFIG systems, the rotor is wounded and the relatively thin wires, compared to the rotor bars in a squirrel-cage induction machine, are not affected by the skin effect to the same extent.

To represent the skin effect phenomenon in a induction machine model, the rotor circuit can be divided into several π-links [16] according to Fig. 5.6.
However, for analysis of transient conditions, in grid connected applications, the rotor circuit impedance presented in Fig. 5.7 is completely satisfactory, as will be demonstrated later on.

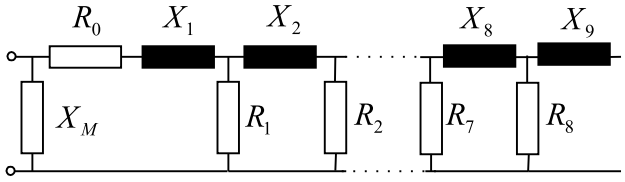

Figure 5.6: Equivalent rotor circuit to take the skin effect into account

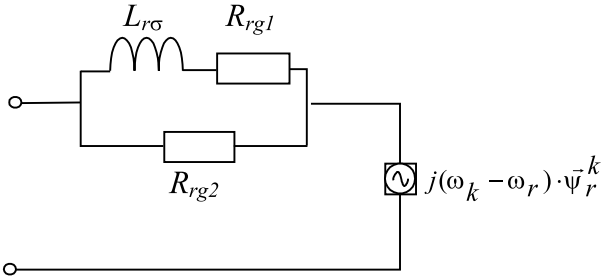

Figure 5.7: Equivalent rotor circuit to take the skin effect into account

In Fig. 5.8 the impedance of the rotor circuit according to Fig. 5.7 and the impedance of the rotor circuit according to Fig. 5.5 (the traditional representation), for different frequencies are shown as well as the measured rotor impedance of the 15kW squirrel-cage induction machine.

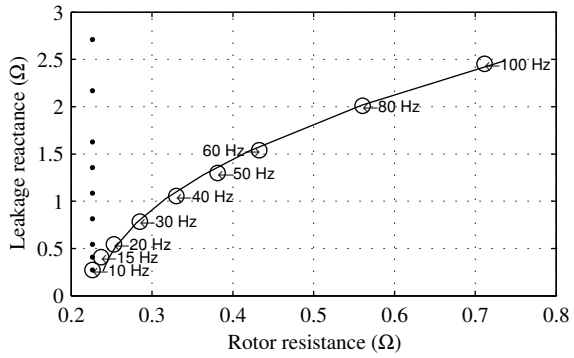

Figure 5.8: Rotor circuit impedance, Circles = measurements, Dots = rotor configuration acc. to Fig. 5.5 and Solid line = rotor circuit configuration acc. to Fig. 5.7.

It can be noted that the agreement is excellent when using the rotor winding representation presented in Fig. 5.7. The parameters in the parallel branch in the rotor circuit can be determined by using a curve fitting method (e.g. Least square method).

Incorporation of the Effect of Saturation

At high currents, the leakage flux paths are affected by saturation. In Fig. 5.9 and in Fig. 5.10 the short circuit inductance (same as the leakage inductance of the Γ-model) and the short-circuit rotor resistance is presented as a function of frequency for three

different current levels. It can be noted that the characteristic of the short circuit inductance is rather independent of the frequency, whereas the effect of saturation of the short circuit inductance is evident. The values decrease quickly as the current level changes from 60 to 90 to 120A. The resistance however, is rather independent of the current level, but changes a lot due to the skin effect.

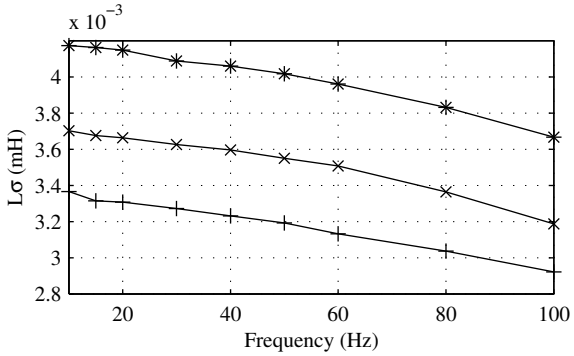

Figure 5.9: The short circuit inductance as a function of frequency at different current levels.

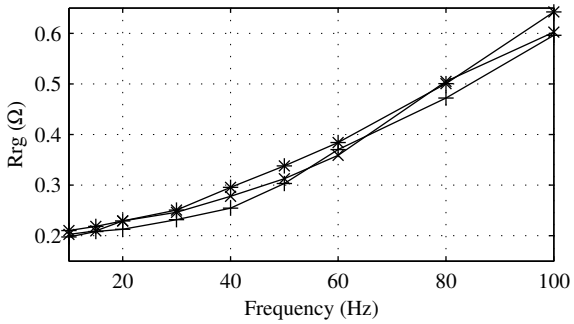

Figure 5.10: The short circuit resistance as a function of frequency at different current levels.

The current dependency of the rotor parameters is here represented by a variable inductance, $L_{r\sigma 0}$, and a variable resistance, R_{rg0}, placed in the equivalent circuit of the rotor. This is shown in Fig. 5.11.

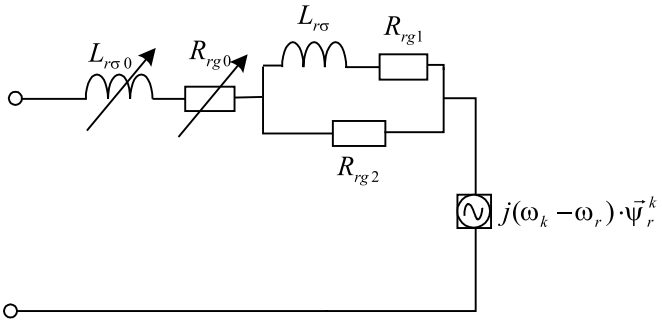

Figure 5.11: The equivalent rotor circuit as the saturation of the leakage flux path and the skin effect are considered.

In order to determine the current dependent parameters without the influence of the skin effect, locked-rotor tests can be done at rather low frequencies. The effect of saturation and the skin effect can however not be completely separated from each other, since measurements show a certain degree of dependency. However, as will be shown later, the separation is made without affecting the degree of accuracy very much.

5.3.2 An Advanced Induction Machine Model

The complete model proposed in this thesis, which is to be used for short-circuit calculations, is presented in Fig. 5.12. The model is similar to the previous presented Γ-model, but the rotor circuit has been replaced with the rotor circuit according to Fig. 5.11. As can be noted, a circulating current is introduced in the parallel branch, which will give rise to an additional complex differential equation.

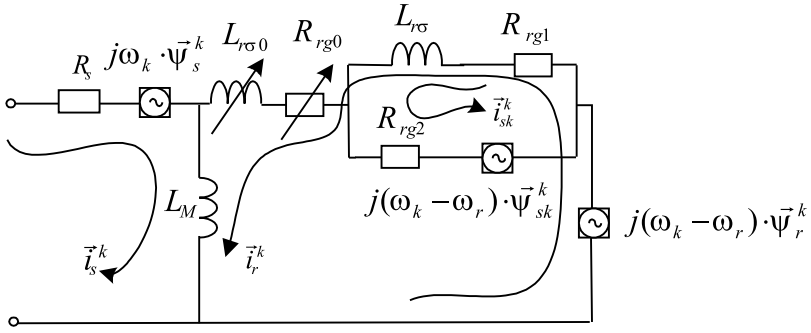

Figure 5.12: The advanced two axis Γ-model equivalent circuit.

Implementation of the induction machine model can for instance be done by using a state-space equation according to

$$\dot{\mathbf{x}} = \mathbf{A}\mathbf{x} + \mathbf{B}\mathbf{u}. \tag{5.47}$$

The circuit differential equation can be written as

$$\mathbf{U} = \mathbf{R}\mathbf{x} + \mathbf{L}\frac{d\mathbf{x}}{dt} \tag{5.48}$$

or put in the state-space form

$$\frac{d\mathbf{x}}{dt} = \mathbf{U}\mathbf{L}^{-1} - \mathbf{R}\mathbf{L}^{-1}\mathbf{x} \tag{5.49}$$

where $\mathbf{U}$ is a column vector containing input signals, $\mathbf{R}$ is the resistance matrix, $\mathbf{L}$ is the inductance matrix and $\mathbf{x}$ is a column vector vector representing the continuously changing variables referred to as states. The vector of input signals, the state vector and the state vector derivatives can, for the model in Fig. 5.12, be expressed as

$$\mathbf{U} = \begin{bmatrix} u_s^x \\ u_s^y \\ u_r^x \\ u_r^y \\ u_{sk}^x \\ u_{sk}^y \\ T_m \end{bmatrix} \quad \mathbf{x} = \begin{bmatrix} i_s^x \\ i_s^y \\ i_r^x \\ i_r^y \\ i_{sk}^x \\ i_{sk}^y \\ \omega_r \end{bmatrix} \quad \frac{d\mathbf{x}}{dt} = \begin{bmatrix} \frac{di_s^x}{dt} \\ \frac{di_s^y}{dt} \\ \frac{di_r^x}{dt} \\ \frac{di_r^y}{dt} \\ \frac{di_{sk}^x}{dt} \\ \frac{di_{sk}^y}{dt} \\ \frac{d\omega_r}{dt} \end{bmatrix}$$

where u represents voltage, i current and T_m the mechanical torque. The superscripts, x and y, denotes the real and the imaginary part of the two axis vector model respectively. Further, the subscripts s, r and sk denote the stator, the rotor and the skin effect branch respectively, see Fig. 5.12. The identification of the matrix $\mathbf{R}$ and $\mathbf{L}$ can easily be accomplished by means of the fundamental equations, derived and described in the following.

For an arbitrary reference frame, the stator voltage can according to (5.16) be expressed as

$$\vec{u}_s^k = R_s\vec{i}_s^k + \frac{d\vec{\psi}_s^k}{dt} + j\omega_k\vec{\psi}_s^k \tag{5.50}$$

Moreover, the rotor voltage can be expressed as

$$\vec{u}_r^k = (R_{rg0} + R_{rg1})\vec{i}_r^k + R_{rg1}\vec{i}_{sk}^k + \frac{d\vec{\psi}_r^k}{dt} + j(\omega_k - \omega_r)\vec{\psi}_r^k \tag{5.51}$$

which looks a bit more complicated than (5.17) due to the incorporation of the skin-effect phenomenon.

Finally, the additional equation of the skin effect branch is expressed according

$$\vec{u}_{sk}^k = (R_{rg1} + R_{rg2})\vec{i}_{sk}^k + R_{rg1}\vec{i}_r^k + \frac{d\vec{\psi}_{sk}^k}{dt} + j(\omega_k - \omega_r)\vec{\psi}_{sk}^k. \tag{5.52}$$

Further, the flux linkages can be expressed as

$$\vec{\psi}_s^k = L_M\vec{i}_s^k + L_M\vec{i}_r^k \tag{5.53}$$
$$\vec{\psi}_r^k = L_M\vec{i}_s^k + (L_{r\sigma} + L_M + L_{r\sigma 0})\vec{i}_r^k + L_{r\sigma}\cdot\vec{i}_{sk}^k \tag{5.54}$$
$$\vec{\psi}_{sk}^k = L_{r\sigma}\vec{i}_{sk}^k + L_{r\sigma}\vec{i}_r^k \tag{5.55}$$

and by deriving these three equations we obtain

$$\frac{d\vec{\psi}_s^k}{dt} = L_M\frac{d\vec{i}_s^k}{dt} + L_M\frac{d\vec{i}_r^k}{dt} \tag{5.56}$$
$$\frac{d\vec{\psi}_r^k}{dt} = L_M\frac{d\vec{i}_s^k}{dt} + (L_{r\sigma} + L_M)\frac{d\vec{i}_r^k}{dt} + \frac{d(L_{r\sigma 0}\cdot\vec{i}_r^k)}{dt} + L_{r\sigma}\frac{d\vec{i}_{sk}^k}{dt} \tag{5.57}$$
$$\frac{d\vec{\psi}_{sk}^k}{dt} = L_{r\sigma}\frac{d\vec{i}_{sk}^k}{dt} + L_{r\sigma}\frac{d\vec{i}_r^k}{dt}. \tag{5.58}$$

As can be noted (5.57) contains the time derivative of the leakage inductance ($dL_{r\sigma 0}/dt$).

$$\frac{d(L_{r\sigma 0}\cdot\vec{i}_r^k)}{dt} = \frac{dL_{r\sigma 0}}{dt}\vec{i}_r^k + L_{r\sigma 0}\frac{d\vec{i}_r^k}{dt} \tag{5.59}$$

but by introducing $d|i_r|/d|i_r|$, (5.59) can be rewritten as

$$\frac{d(L_{r\sigma 0}\cdot\vec{i}_r^k)}{dt} = L_{r\sigma 0}\frac{d\vec{i}_r^k}{dt} + \vec{i}_r^k\frac{dL_{r\sigma 0}}{d|i_r|}\frac{d|i_r|}{dt} \tag{5.60}$$

Further, $d|i_r|/dt$ can be written as

$$\frac{d|i_r|}{dt} = \frac{d}{dt}\sqrt{(i_r^x)^2 + (i_r^y)^2} \tag{5.61}$$

and if the derivation is performed, the following expression is obtained

$$\frac{d|i_r|}{dt} = \frac{i_r^x \frac{di_r^x}{dt} + i_r^y \frac{di_r^y}{dt}}{|i_r|} \tag{5.62}$$

Hence, equation (5.59) can written according to

$$\frac{d(L_{r\sigma 0} \cdot \vec{i}_r^k)}{dt} = L_{r\sigma 0} \frac{d\vec{i}_r^k}{dt} + \vec{i}_r^k \frac{dL_{r\sigma 0}}{d|i_r|} \left[\frac{i_r^x \frac{di_r^x}{dt} + i_r^y \frac{di_r^y}{dt}}{|i_r|} \right] \tag{5.63}$$

which, by separating the equation (5.63) into a real and a imaginary part, can be expressed in the following way

$$L_{r\sigma 0}^x = L_{r\sigma 0} + \frac{(i_r^x)^2}{|i_r|} \frac{dL_{r\sigma 0}}{d|i_r|} \tag{5.64}$$

$$L_{r\sigma 0}^y = L_{r\sigma 0} + \frac{(i_r^y)^2}{|i_r|} \frac{dL_{r\sigma 0}}{d|i_r|} \tag{5.65}$$

$$L_{r\sigma 0}^{xy} = \frac{i_r^x i_r^y}{|i_r|} \cdot \frac{dL_{r\sigma 0}}{d|i_r|} \tag{5.66}$$

Finally, the speed equation of the induction machine, which can be expressed according to (5.67), where T_e is the electromagnetic torque.

$$T_m = T_e - \frac{J}{p} \frac{d\omega_r}{dt} \tag{5.67}$$

T_e can further be expressed as

$$T_e = p(\vec{\psi}_s^k (\vec{i}_s^k)^*) \tag{5.68}$$

where p is number of pole-pairs. ω_r is the angular speed expressed in electrical rad/s.

The resistance matrix, R, and the inductance matrix, L, for the advanced two axis induction machine can finally be identified and expressed according to the following

$$\mathbf{R} = \begin{bmatrix} (R_s & -\omega_k L_M & 0 \\ \omega_k L_M & R_s & \omega_k L_M \\ 0 & -(\omega_k - \omega_r) L_M & R_{rg0} + R_{rg1} \\ (\omega_k - \omega_r) L_M & 0 & (\omega_k - \omega_r)(L_{r\sigma} + L_{r\sigma 0} + L_M) \\ 0 & 0 & R_{rg1} \\ 0 & 0 & (\omega_k - \omega_r) L_{r\sigma} \\ -\frac{3}{2} p L_M i_{ry} & \frac{3}{2} p L_M i_{rx} & 0 \end{bmatrix}$$

$$\begin{bmatrix} -\omega_k L_M & 0 & 0 & 0 \\ 0 & 0 & 0 & 0 \\ -(\omega_k-\omega_r)(L_{r\sigma}+L_{r\sigma 0}+L_M) & R_{rg1} & -(\omega_k-\omega r)L_{r\sigma} & 0 \\ R_{rg0}+R_{rg1} & (\omega_k-\omega_r)L_{r\sigma} & R_{rg1} & 0 \\ -(\omega_k-\omega_r)L_{r\sigma} & R_{rg1}+R_{rg2} & -(\omega_k-\omega_r)L_{r\sigma} & 0 \\ R_{rg1} & (\omega_k-\omega_r)L_{r\sigma} & R_{rg1}+R_{rg2} & 0 \\ 0 & 0 & 0 & 0 \end{bmatrix}$$

$$\mathbf{L} = \begin{bmatrix} L_M & 0 & L_M & 0 & 0 & 0 & 0 \\ 0 & L_M & 0 & L_M & 0 & 0 & 0 \\ L_M & 0 & L_{r\sigma}+L_M+L^x_{r\sigma 0} & L^{xy}_{r\sigma 0} & L_{r\sigma} & 0 & 0 \\ 0 & L_M & L^{xy}_{r\sigma 0} & L_{r\sigma}+L_M+L^y_{r\sigma 0} & 0 & L_{r\sigma} & 0 \\ 0 & 0 & L_{r\sigma} & 0 & L_{r\sigma} & 0 & 0 \\ 0 & 0 & 0 & L_{r\sigma} & 0 & L_{r\sigma} & 0 \\ 0 & 0 & 0 & 0 & 0 & 0 & -\dfrac{J}{p} \end{bmatrix}$$

5.3.3 Slip-Ringed Induction Machine

The slip-ringed induction machine is used in the DIFG wind turbine system, Fig. 5.13. The generator has a wounded rotor supplied by a power electronic converter, which implies that the rotor voltage can be controlled.

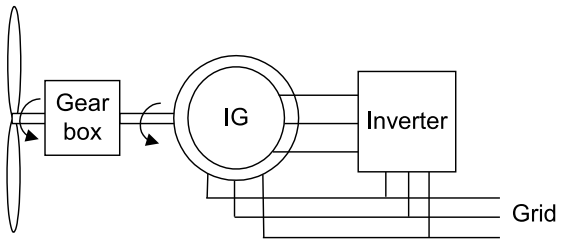

Figure 5.13: Variable-speed doubly-fed induction generator system.

The equations describing the slip-ringed induction machine, is identical with the general equations describing the squirrel-cage induction machine. The only difference is that $\vec{u}_r^k \neq 0$.

$$\vec{u}_s^k = R_s \vec{i}_s^k + \frac{d\vec{\psi}_s^k}{dt} + j\omega_k \vec{\psi}_s^k \tag{5.69}$$

$$\vec{u}_r^k = R_r \vec{i}_r^k + \frac{d\vec{\psi}_r^k}{dt} + j(\omega_k - \omega_r)\vec{\psi}_r^k. \tag{5.70}$$

For the slip-ringed induction machine the rotor voltage is adjusted to achieve a desired slip or torque and the following simplified expressions describes the relationship

between the rotor and the stator voltage ($\vec{u}_s$, $\vec{u}_r$), the slip, s and the torque, T_e [1]. The slip can be described according to (5.71)

$$s = \frac{\omega - \omega_r}{\omega} \approx |\frac{\vec{u}_r}{\vec{u}_s}| \tag{5.71}$$

and the torque according to (5.72)

$$T_e = P_m \frac{p}{(1-s)\omega} \tag{5.72}$$

where p is the number of pole pairs, P_m the mechanical power and ω the synchronous angular frequency. ω_r is the angular frequency of the rotor.
The objective of this thesis is to study the response of severe network fault conditions, but as the slip-ringed induction machine is considered, even disturbances are of great interest and importance.

For severe faults, the inverter is protected from over voltages by a crow-bar that short circuits the rotor windings. The behavior of the slip-ringed induction machine can therefor be considered similar to that of the squirrel-cage induction machine and the equations presented in previous section may be used. In Fig. 7.12 a schematic figure of the DFIG system is presented, indicating the placement of the crowbar short-circuit device.

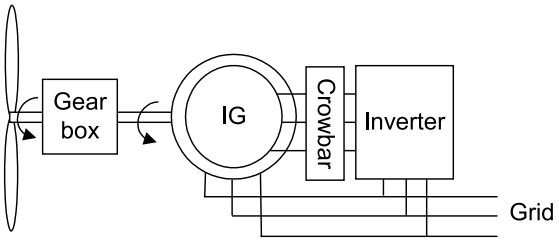

Figure 5.14: DFIG system including the crowbar short-circuit device.

However, the crowbar short-circuit device may operate even if the supply voltage only deviates partly from the rated voltage. Depending on the operating conditions of the DFIG system, the generator can either be running at super-synchronous or sub-synchronous speed. If the crowbar operation is initiated, it may lead to a large consumption of reactive power and high currents due to the acceleration/deacceleration of the induction generator. This fact has led to that the DFIG is disconnected as soon as possible, after a crowbar operation has been initiated and the rotor windings have been short circuited. It should be pointed out that this is a very important problem, and that the manufacturers are working with a solution which will make at least a short-term voltage drop ride through possible.

5.4 Three Phase Model of the Induction Machine

A three-phase model is more useful then the two-axis representation of the induction machine when it comes to unsymmetrical operating conditions. Each phase winding in both stator and rotor are represented separately where the angle displacement between the windings in both the stator and the rotor are 120° in similarity to the real machine, see Fig. 5.15. In the two axis representation the angle between the two fictive perpendicular windings is 90°.

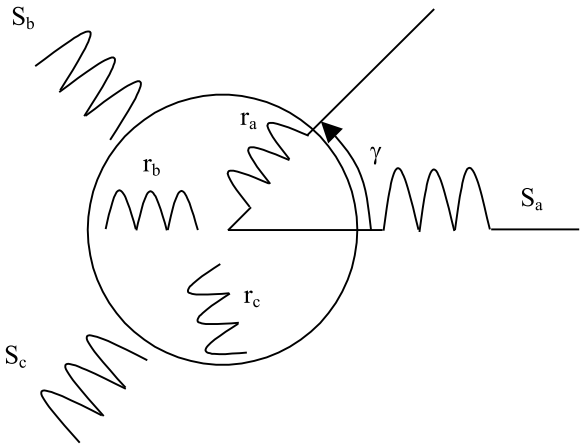

Figure 5.15: The three phase representation of a induction machine windings.

The effect of saturation is included in the same way as for the advanced xy-model, i.e. the saturation in the three different phases are considered to be equal. The simplification imply the possibility to calculate the parameters in the same way as for the two-axis model, where the derivative, $dL_{r\lambda}/di$, is calculated exactly in the same way as in equation 5.62, implying that a transformation from the three phase system to the two-axis system is done, using the real and the imaginary components to identify the accurate parameters. This is however accurate as long as the machine is exposed to symmetrical operating condition or disturbances.

The skin effect is taken into consideration exactly in the same way as for the two-axis model, in which a parallel branch of a resistance and two inductances are incorporated in the rotor circuit, Fig. 5.11.

Each winding has a main inductance, L_h. The mutual inductance between two phase windings is

$$M = L_h \cos(\vartheta) \tag{5.73}$$

where ϑ is the angle between two windings. Between phase winding a and phase winding b, ϑ is equal to $2\pi/3$, and between phase winding a and c, the angle is equal

to $4\pi/3$. The mutual inductance between phase winding a and one of the two other stator phase windings can than be calculated according to (5.73), which yields

$$M = -\frac{L_h}{2}. \tag{5.74}$$

The flux in phase a can without linked rotor fluxes, be calculated according to,

$$\psi_{sa} = (L_h + L_{s\lambda})i_{sa} + Mi_{sb} + Mi_{sc} \tag{5.75}$$

and if (5.74) is inserted in this expression, the result becomes

$$\psi_{sa} = (L_h + L_{s\lambda})i_{sa} - \frac{L_h}{2}i_{sb} - \frac{L_h}{2}i_{sc}. \tag{5.76}$$

The same yields for the rotor windings.

In a system where the neutral is not connected, i_{sa} is equal to $-i_{sb} - i_{sc}$, which yields if inserted in (5.76)

$$\psi_{sa} = (L_h + L_{s\lambda})i_{sa} + \frac{L_h}{2}i_{sa} = (\frac{3}{2}L_h + L_{s\lambda})i_{sa} \tag{5.77}$$

where $\frac{3}{2}L_h$ is equal to the familiar variable L_m, which is the magnetizing inductance in a wye-equivalent representation of the induction machine.

If the three-phase model should account for the possibility where $i_{sa} + i_{sb} + i_{sc} \neq 0$, a simplification according to (5.77)can not be used. If consideration is taken to that the rotor also has three phase windings located 120° apart and the angle towards the stator is γ, the stator flux can be expressed according to (5.78)

$$\begin{aligned} \psi_{sa} &= (L_h + L_{s\lambda})i_{sa} - \frac{L_h}{2}i_{sb} - \frac{L_h}{2}i_{sc} + L_h i_{ra}\cos(\gamma) + L_h i_{rb}\cos(\frac{2\pi}{3} + \gamma) \\ &\quad + L_h i_{rc}\cos(\frac{4\pi}{3} + \gamma). \end{aligned} \tag{5.78}$$

In Fig. 5.16 a simplified equivalent circuit is presented to have a reference for all the parameters.

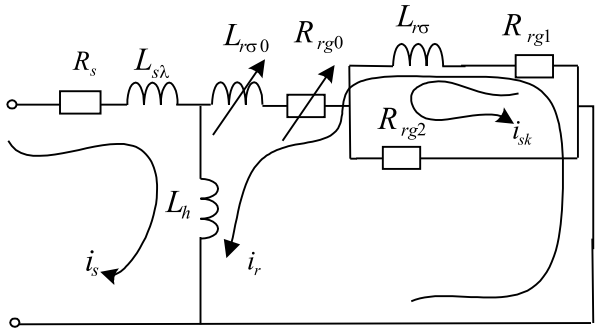

Figure 5.16: Equivalent circuit for the three phase representation, valid for all three phase quantities.

The stator voltage of phase a, which is familiar from previous chapters, can be written according to

$$u_{sa} = R_s i_{sa} + \frac{d\psi_{sa}}{dt}. \tag{5.79}$$

The time derivative of (5.78) can further be expressed as

$$\begin{aligned}\frac{d\psi_{sa}}{dt} &= (L_h + L_{s\lambda})\frac{di_{sa}}{dt} - \frac{L_h}{2}\frac{di_{sb}}{dt} - \frac{di_{sc}}{dt}\frac{L_h}{2} - L_h i_{ra}\frac{d\gamma}{dt}\sin(\gamma) \\ &\quad + L_h\frac{di_{ra}}{dt}\cos\gamma - L_h i_{rb}\frac{d\gamma}{dt}\sin(\frac{2\pi}{3}+\gamma) + L_h\frac{di_{rb}}{dt}\cos(\frac{2\pi}{3}+\gamma) \\ &\quad - L_h i_{rc}\frac{d\gamma}{dt}\sin(\frac{4\pi}{3}+\gamma) + L_h\frac{di_{rc}}{dt}\cos(\frac{4\pi}{3}+\gamma)\end{aligned} \tag{5.80}$$

where $d\gamma/dt = w_r$. For simplicity, the following variables are now introduced

$$\begin{aligned} B1 &= \sin(\gamma) & A1 &= \cos(\gamma) \\ B2 &= \sin(2\pi/3+\gamma) & A2 &= \cos(2\pi/3+\gamma) \\ B3 &= \sin(4\pi/3+\gamma) & A3 &= \cos(4\pi/3+\gamma) \end{aligned}$$

and finally, the stator and rotor equations can then be expressed according to

$$\begin{aligned} u_{sa} &= R_s i_{sa} - X_h B_1 i_{ra} - X_h B_2 i_{rb} - X_h B_3 i_{rc} + (L_{s\lambda} + L_h)\frac{di_{sa}}{dt} - \frac{L_h}{2}\frac{di_{sb}}{dt} \\ &\quad - \frac{L_h}{2}\frac{di_{sc}}{dt} + A_1 L_h\frac{di_{ra}}{dt} + A_2 L_h\frac{di_{rb}}{dt} + A_3 L_h\frac{di_{rc}}{dt} \end{aligned} \tag{5.81}$$

$$\begin{aligned} u_{sb} &= R_s i_{sb} - X_h B_3 i_{ra} - X_h B_1 i_{rb} - X_h B2 i_{rc} + (L_{s\lambda} + L_h)\frac{di_{sb}}{dt} - \frac{L_h}{2}\frac{di_{sa}}{dt} \\ &\quad - \frac{L_h}{2}\frac{di_{sc}}{dt} + A_3 L_h\frac{di_{ra}}{dt} + A_1 L_h\frac{di_{rb}}{dt} + A_2 L_h\frac{di_{rc}}{dt} \end{aligned} \tag{5.82}$$

$$\begin{aligned} u_{sc} &= R_s i_{sc} - X_h B_2 i_{ra} - X_h B_3 i_{rb} - X_h B1 i_{rc} + (L_{s\lambda} + L_h)\frac{di_{sc}}{dt} - \frac{L_h}{2}\frac{di_{sa}}{dt} \\ &\quad - \frac{L_h}{2}\frac{di_{sb}}{dt} + A_2 L_h\frac{di_{ra}}{dt} + A_3 L_h\frac{di_{rb}}{dt} + A_1 L_h\frac{di_{rc}}{dt} \end{aligned} \tag{5.83}$$

$$
\begin{aligned}
u_{ra} &= -X_h B_1 i_{sa} - X_h B_3 i_{sb} - X_h B_2 i_{sb} + (R_{rg0} + R_{rg1}) i_{ra} + R_{rg1} i_{ska} + A_1 L_h \frac{di_{sa}}{dt} \\
&\quad + A_3 L_h \frac{di_{sb}}{dt} + A_2 L_h \frac{di_{sc}}{dt} + (L_{r\sigma} + L_h) \frac{di_{ra}}{dt} + \frac{d(L_{r\sigma 0} \cdot i_{ra})}{dt} - \frac{L_h}{2} \frac{di_{rb}}{dt} \\
&\quad - \frac{L_h}{2} \frac{di_{rc}}{dt} + L_{r\sigma} \frac{di_{ska}}{dt} \qquad (5.84) \\
u_{rb} &= -X_h B_2 i_{sa} - X_h B_1 i_{sb} - X_h B_3 i_{sb} + (R_{rg0} + R_{rg1}) i_{rb} + R_{rg1} i_{skb} + A_2 L_h \frac{di_{sa}}{dt} \\
&\quad + A_1 L_h \frac{di_{sb}}{dt} + A_3 L_h \frac{di_{sc}}{dt} + (L_{r\sigma} + L_h) \frac{di_{rb}}{dt} + \frac{d(L_{r\sigma 0} \cdot i_{rb})}{dt} - \frac{L_h}{2} \frac{di_{ra}}{dt} \\
&\quad - \frac{L_h}{2} \frac{di_{rc}}{dt} + L_{r\sigma} \frac{di_{skb}}{dt} \qquad (5.85) \\
u_{rc} &= -X_h B_3 i_{sa} - X_h B_2 i_{sb} - X_h B_1 i_{sb} + (R_{rg0} + R_{rg1}) i_{rc} + R_{rg1} i_{skc} + A_3 L_h \frac{di_{sa}}{dt} \\
&\quad + A_2 L_h \frac{di_{sb}}{dt} + A_1 L_h \frac{di_{sc}}{dt} + (L_{r\sigma} + L_h) \frac{di_{rc}}{dt} + \frac{d(L_{r\sigma 0} \cdot i_{rc})}{dt} - \frac{L_h}{2} \frac{di_{ra}}{dt} \\
&\quad - \frac{L_h}{2} \frac{di_{rb}}{dt} + L_{r\sigma} \frac{di_{skc}}{dt} \qquad (5.86)
\end{aligned}
$$

Further, the equations for representing the skin effect branch can be expressed as

$$
\begin{aligned}
u_{ska} &= R_{rg1} i_{ra} + (R_{rg1} + R_{rg2}) i_{ska} + L_{r\sigma} \frac{di_{ra}}{dt} + L_{r\sigma} \frac{di_{iska}}{dt} \\
u_{skb} &= R_{rg1} i_{rb} + (R_{rg1} + R_{rg2}) i_{skb} + L_{r\sigma} \frac{di_{rb}}{dt} + L_{r\sigma} \frac{di_{iskb}}{dt} \qquad (5.87) \\
u_{skc} &= R_{rg1} i_{rc} + (R_{rg1} + R_{rg2}) i_{skc} + L_{r\sigma} \frac{di_{rc}}{dt} + L_{r\sigma} \frac{di_{iskc}}{dt} \qquad (5.88) \\
& \qquad (5.89)
\end{aligned}
$$

The electromagnetic torque for the three-phase induction machine model can be written as

$$
\begin{aligned}
T_e &= -pL_h\big((B_1 i_{ra} + B_2 i_{rb} + B_3 i_{rc}) + (B_1 i_{rb} + B_2 i_{rc} + B3 i_{ra}) + \\
&\quad (B_1 i_{rc} + B_2 i_{ra} + B3 i_{rb})\big) \qquad (5.90)
\end{aligned}
$$

All these equations presented above results in the following resistance matrix

$$\begin{bmatrix}
R_s & 0 & 0 \\
0 & R_s & 0 \\
0 & 0 & R_s \\
-X_h B_1 & -X_h B_3 & -X_h B_2 \\
-X_h B_2 & -X_h B_1 & -X_h B_3 \\
-X_h B_3 & -X_h B_2 & -X_h B_1 \\
0 & 0 & 0 \\
0 & 0 & 0 \\
0 & 0 & 0 \\
-pL_h(B_1 i_{ra} + B_2 i_{rb} + B_3 i_{rc}) & -pL_h(B_1 i_{rb} + B_2 i_{rc} + B_3 i_{ra}) & -pL_h(B_1 i_{rc} + B_2 i_{ra} + B_3 i_{rb}) \\
0 & 0 & 0
\end{bmatrix}$$

$$\begin{bmatrix}
-X_h B_1 & -X_h B_2 & -X_h B_3 & 0 & 0 & 0 & 0 & 0 \\
-X_h B_3 & -X_h B_1 & -X_h B_2 & 0 & 0 & 0 & 0 & 0 \\
-X_h B_2 & -X_h B_3 & -X_h B_1 & 0 & 0 & 0 & 0 & 0 \\
R_{rg1} + R_{rg0} & 0 & 0 & R_{rg1} & 0 & 0 & 0 & 0 \\
0 & R_{rg1} + R_{rg0} & 0 & 0 & R_{rg1} & 0 & 0 & 0 \\
0 & 0 & R_{rg1} + R_{rg0} & 0 & 0 & R_{rg1} & 0 & 0 \\
R_{rg1} & 0 & 0 & (R_{rg1} + R_{rg2}) & 0 & 0 & 0 & 0 \\
0 & R_{rg1} & 0 & 0 & (R_{rg1} + R_{rg2}) & 0 & 0 & 0 \\
0 & 0 & R_{rg1} & 0 & 0 & (R_{rg1} + R_{rg2}) & 0 & 0 \\
0 & 0 & 0 & 0 & 0 & 0 & 0 & 0 \\
0 & 0 & 0 & 0 & 0 & 0 & -1 & 0
\end{bmatrix}$$

and the following inductance matrix

$$\begin{bmatrix}
(L_{s\lambda} + L_h) & -L_h/2 & -L_h/2 & A_1 L_h & A_2 L_h \\
-L_h/2 & (L_{s\lambda} + L_h) & -L_h/2 & A_3 L_h & A_1 L_h \\
-L_h/2 & -L_h/2 & (L_{s\lambda} + L_h) & A_2 L_h & A_3 L_h \\
A_1 L_h & A_3 L_h & A_2 L_h & (L_{r\sigma 0} + L_h + L_{r\sigma} + L_{\sigma A} i_{ra}) & L_{\sigma B} i_{ra} - L_h/2 \\
A_2 L_h & A_1 L_h & A_3 L_h & L_{\sigma A} i_{rb} - L_h/2 & (L_{r\sigma} + L_h + L_{r\sigma 0} + L_{\sigma B} i_{rb}) \\
A_3 L_h & A_2 L_h & A_1 L_h & L_{\sigma A} i_{rc} - L_h/2 & L_{\sigma B} i_{rc} - L_h/2 \\
0 & 0 & 0 & L_{r\sigma} & 0 \\
0 & 0 & 0 & 0 & L_{r\sigma} \\
0 & 0 & 0 & 0 & 0 \\
0 & 0 & 0 & 0 & 0 \\
0 & 0 & 0 & 0 & 0
\end{bmatrix}$$

$$
\begin{bmatrix}
A_3 L_h & 0 & 0 & 0 & 0 & 0 \\
A_2 L_h & 0 & 0 & 0 & 0 & 0 \\
A_1 L_h & 0 & 0 & 0 & 0 & 0 \\
L_{\sigma C} i_{ra} - L_h/2 L_{r\sigma} & 0 & 0 & 0 & 0 & \\
L_{\sigma C} i_{rb} - L_h/2 & 0 & L_{r\sigma} & 0 & 0 & 0 \\
(L_{r\sigma} + L_h + L_{r\sigma 0} + L_{\sigma C} i_{rc}) & 0 & 0 & L_{r\sigma} & 0 & 0 \\
0 & L_{r\sigma} & 0 & 0 & 0 & 0 \\
0 & 0 & L_{r\sigma} & 0 & 0 & 0 \\
L_{r\sigma} & 0 & 0 & L_{r\sigma} & 0 & 0 \\
0 & 0 & 0 & 0 & -J/p & 0 \\
0 & 0 & 0 & 0 & 0 & 1
\end{bmatrix}
$$

where $L_{\sigma A}$, $L_{\sigma B}$ and $L_{\sigma C}$ are the results from the derivation of the terms $d(L_{\sigma 0} \cdot di_r a)/dt$, $d(L_{\sigma 0} \cdot di_r b)/dt$ and $d(L_{\sigma 0} \cdot di_r c)/dt$ in (5.84), (5.85) and (5.86). All according to the same procedure as in (5.59) - (5.66), which is again is presented below.

$$
\begin{aligned}
\frac{d(L_{r\sigma} i_{ra})}{dt} &= L_{r\sigma} \cdot \frac{di_{ra}}{dt} + i_{ra} \cdot \frac{dL_{r\sigma}}{dt} && (5.91) \\
\frac{dL_{r\sigma}}{dt} &= \frac{dL_{r\sigma}}{d|ir|} \cdot \frac{d|i_r|}{dt} && (5.92)
\end{aligned}
$$

where $d|ir|/dt$ can be described according to (in accordance with (5.8)

$$
\begin{aligned}
\frac{d|i_r|}{dt} &= \frac{d}{dt}\sqrt{i_{ra}^2 + \frac{1}{3}\big(i_{rb} - i_{rc}\big)^2} && (5.93) \\
&= \frac{d}{dt}\sqrt{i_{ra}^2 + \frac{1}{3}\big(i_{rb}^2 - 2 i_{rb} i_{rc} + i_{rc}^2\big)} \\
&= \frac{1}{2|i_r|} \cdot \big[2 i_{ra}\frac{di_{ra}}{dt} + \frac{2}{3} i_{rb}\frac{di_{rb}}{dt} - \frac{2}{3}\big(i_{rb}\frac{di_{rc}}{dt} + i_{rc}\frac{di_{rb}}{dt}\big) + \frac{2}{3} i_{rc}\frac{di_{rc}}{dt}\big] \\
&= \frac{i_{ra}}{|i_r|}\frac{di_{ra}}{dt} + \frac{1}{3}\frac{(i_{rb} - i_{rc})}{|i_r|}\frac{di_{rb}}{dt} + \frac{1}{3}\frac{(i_{rc} - i_{rb})}{|i_r|}\frac{di_{rc}}{dt}.
\end{aligned}
$$

Finally, $L_{\sigma A}$, $L_{\sigma A}$ and $L_{\sigma A}$, can be written according to

$$
\begin{aligned}
L_{\sigma A} &= [L_{r\sigma} + \frac{i_{ra}^2}{|i_r|}\frac{dL_{r\sigma}}{d|i_r|}] && (5.94) \\
L_{\sigma B} &= [\frac{1}{3}\frac{(i_{rb} - i_{rc}) i_{ra}}{|i_r|}\frac{dL_{r\sigma}}{d|i_r|}] && (5.95) \\
L_{\sigma C} &= [\frac{1}{3}\frac{(i_{rc} - i_{rb}) i_{ra}}{|i_r|}\frac{dL_{r\sigma}}{d|i_r|}]. && (5.96)
\end{aligned}
$$

Chapter 6

Experimental set-up and Parameter Identification

In the previous chapter was described how the machine parameters vary due to skin effect and leakage flux saturation and how these two phenomena could be incorporated into the models, in order predict the dynamic behavior and the fault current response. Unfortunately there is no shortcut when it comes to determining the parameters and how the parameters vary due to changing current and frequency. As mentioned earlier, one has to either accomplish advanced FEM computations, with respect to the geometrical design of the generator, or perform extensive measurements, which have been done in this thesis.

There are mainly three different experimental set-ups that have been used. One for steady-state measurements, which has been used for the parameter identification of the induction machine and one for dynamic measurements which was used in order to apply disturbances to the induction machine. Finally, an experimental set-up for the investigation of the response of the slip-ringed induction machine, due to network disturbances and resulting crow-bar action, has been used.

Since the objective of the thesis is to predict the currents arising from severe fault conditions, the rotor and stator resistances and the leakage inductances are of great interest. To account for phenomena, such as skin effect and saturation of the leakage flux path, the tests have to be done for different frequencies and voltage (current) levels respectively.

6.1 Steady State Measurements

To identify the steady state parameters of an induction machine, a no-load test, a locked-rotor test and measurement of the stator resistance have to be made. For many cases where an induction machine model is needed, one set of parameters valid for 50Hz and rated current are satisfactory. However, for advanced calculations a more detailed model, such as the model presented in chapter 5 can be required and as already

been mentioned, the identification measurements become more extensive. In Fig. 6.1 the connection used for the parameter identification is presented. The connection is used for symmetrical three phase measurements (besides three phase short circuit measurements), such as starts, locked rotor tests and no-load tests.

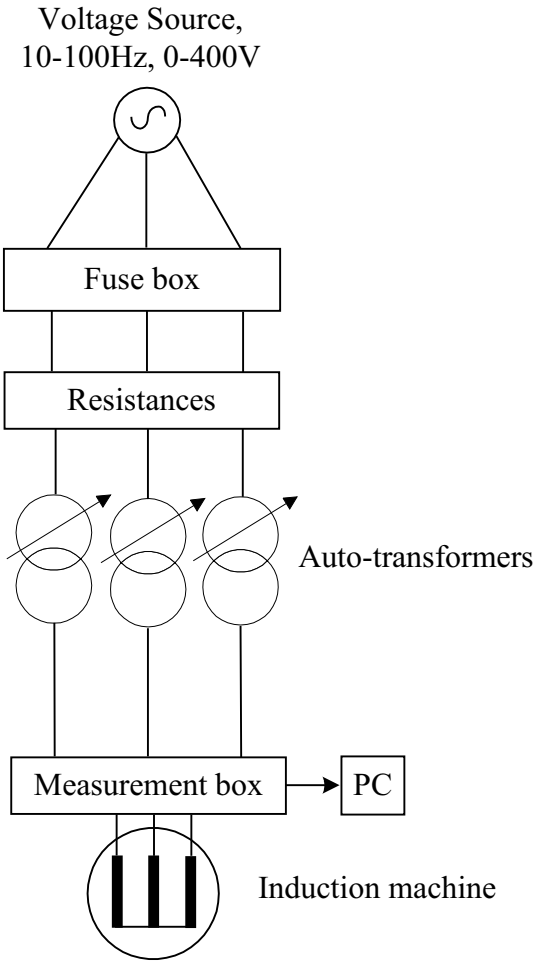

Figure 6.1: The measurement setup for steady state measurements.

The voltage sources have been of different types. To start with, the strong 50Hz 230V and 400V grid, were used. These two different voltage levels are obtained by transformation from the 10kV distribution network, with no other separate objects connected, apart from the induction machine. Resistors connected in series were in this case used to provide the possibility to adjust the voltage level. For some cases auto-transformers were used to obtain various voltages at the fixed frequency of 50Hz.

An electrically magnetized speed controlled synchronous machine was used at some occasions, which had the advantage that a voltage with a very low harmonic distortion could be delivered and it could also provide us with the possibility to change the frequency as well as the voltage magnitude in a broad range. A drawback however, was the inability of the synchronous machine to maintain a constant voltage magnitude during transient fault conditions and it was thus only useful for steady state parameter

identification measurements.

The measurement interface consist of voltage and current transducers, AD210 BN and LEM-modules with a bandwidth of several kHz. The sampling frequency was set to 5 kHZ.

In Fig. 6.2 - Fig. 6.5 pictures of the different components in the measurement set-up are shown.

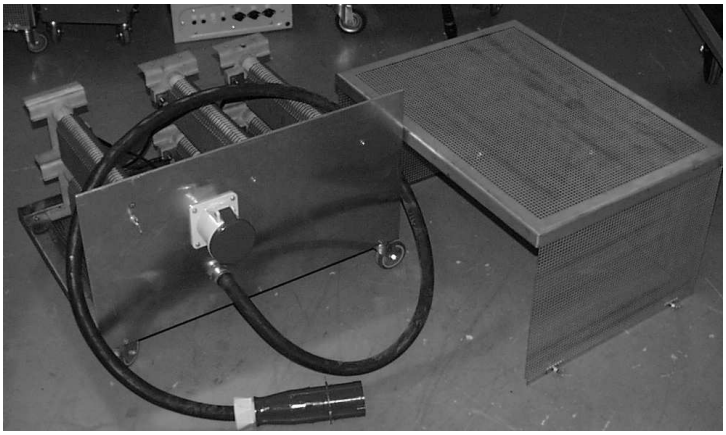

Figure 6.2: Three phase resistances that sometimes were used to limit the applied voltage.

Figure 6.3: The photo show the auto-transformers. The 200A input connections can be noted on the short side of the auto-transformers and the different levels of out-put voltage can be noted on the front side on the autotransformer in the middle of the picture.

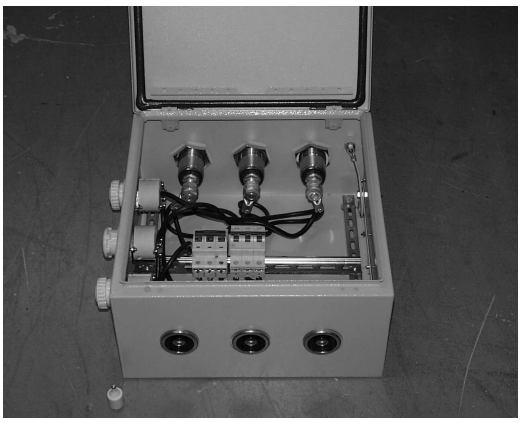

Figure 6.4: Fuse box used to protect the bigger more expensive fuses that protects the voltage sources.

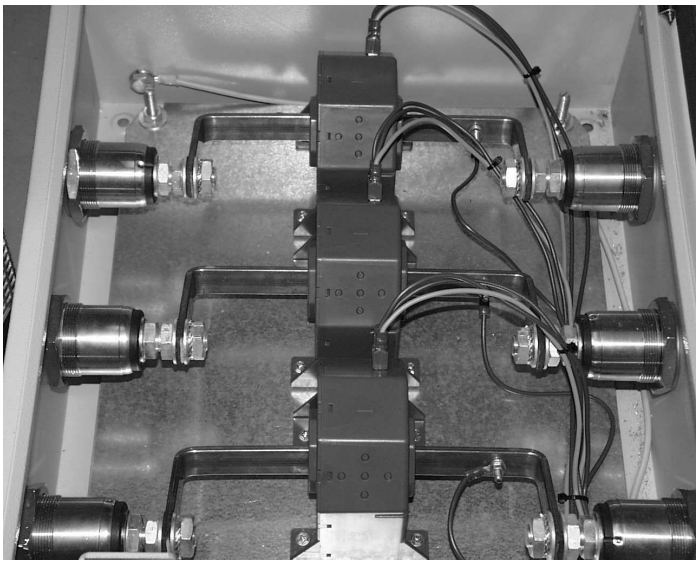

Figure 6.5: Measurement box with the LEM modules for current measurement. The box also includes the voltage measurement cards (not shown in the picture).

Steady-state measurements have been performed on a 15kW squirrel -cage induction machine and on a 22kW slip-ringed induction machine, where the 15kW induction machine has been used as the main object. The manufacturer data of the 15kW machine is presented in Table 6.1 and the machine is shown in Fig. 6.6.

Table 6.1: General parameter values given by the manufacturer for the 15kW squirrel-cage induction machine.

R_s	Stator resistance	$0,18\Omega$
R_r	Rotor resistance	$0,19\Omega$
L_m	Magnetizing inductance	$42,6mH$
$L_{s\lambda}$	Stator leakage inductance	$2,55mH$
$L_{r\lambda}$	Rotor leakage inductance	$2,07mH$
J	Inertia	$0,205kgm^2$
U_n	Rated voltage	$380V$
f	Frequency	$50Hz$
p	Number pole pairs	3
n	Nominal speed	$970rpm$

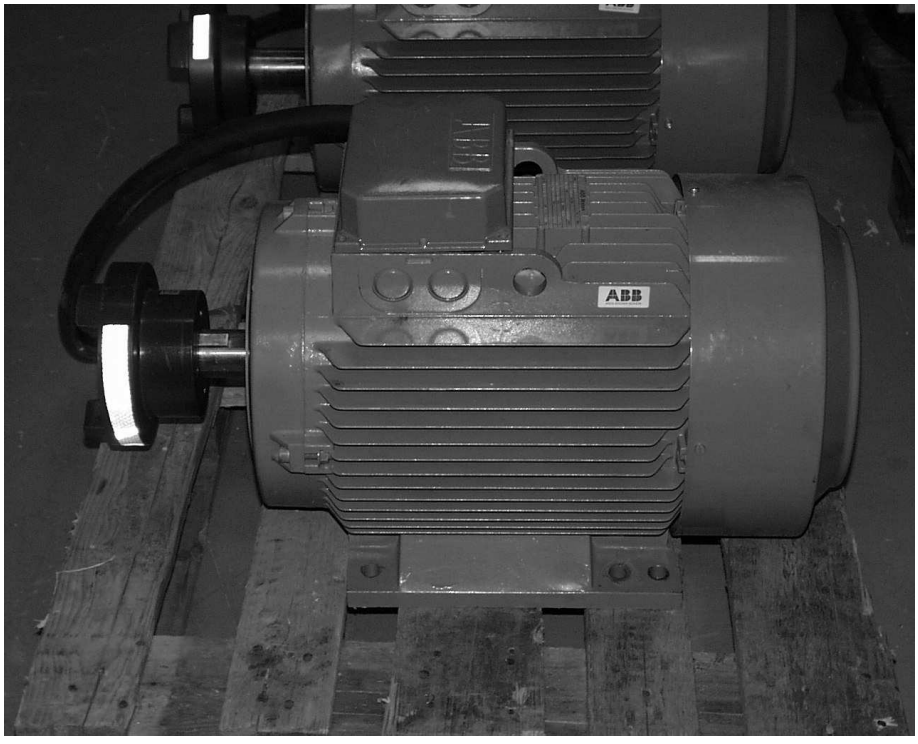

Figure 6.6: A picture of the 15kW squirrel-cage induction machine.

The same parameters for the 22kW slip-ringed induction machine is presented in Table 6.2 and a photo of the 22kW slip-ringed induction machine is presented in Fig. 6.7

Table 6.2: General parameter values given by the manufacturer for the 22kW slip-ringed induction machine.

R_s	Stator resistance	$0,115\Omega$
R_r	Rotor resistance	$0,184\Omega$
L_m	Magnetizing inductance	$46,6mH$
$L_{s\lambda}$	Stator leakage inductance	$1,65mH$
$L_{r\lambda}$	Rotor leakage inductance	$1,68mH$
J	Inertia	$0,534kgm^2$
U_n	Rated voltage	$400V$
f	Frequency	$50Hz$
p	Number of pole pairs	2
n	Nominal speed	$1440rpm$

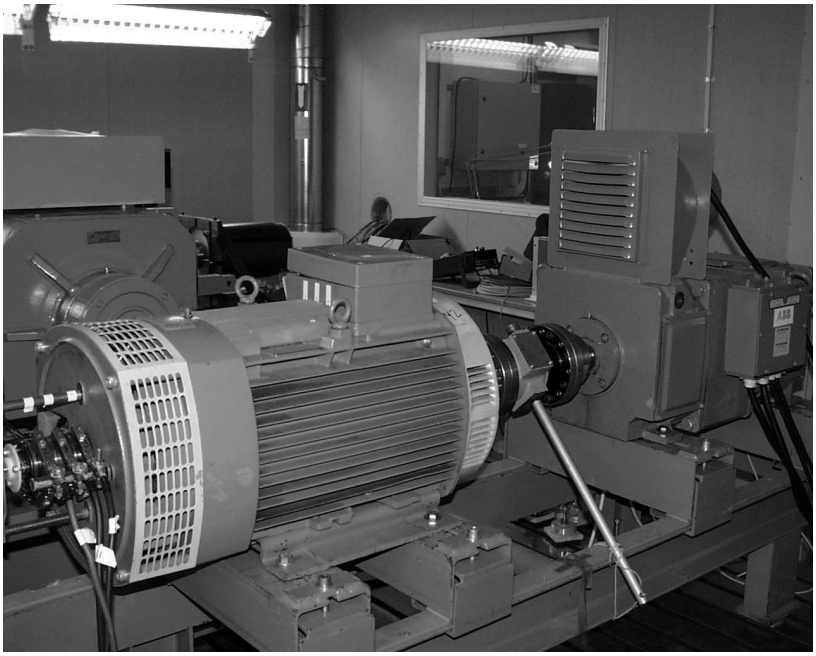

Figure 6.7: A picture of the 22kW slip-ringed induction machine also showing the DC machine.

The parameters presented in the tables above are related to the conventional T-model or the Park model. A simple equivalent circuit is presented in Fig. 6.8, where all the parameters given by the manufacturer are shown.

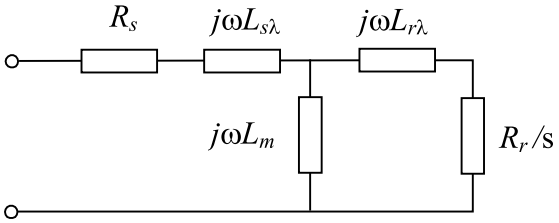

Figure 6.8: Classical equivalent circuit of the induction machine.

6.1.1 No Load Test

The no-load test is accomplished by applying voltage to the induction machine, which will start to rotate. When the machine has reached the final speed, the voltages and the currents are measured in each phase. From this kind of measurement the magnetizing inductance can be determined as a function of the no-load voltage (its variation has however a little influence on the dynamic behavior of the induction machine). In Table 6.3 L_M is presented together with the no-load voltage, the no-load current and the flux in p.u.. Note that the measurement is made at 40Hz, which was done to reach a higher flux level without exceeding the nominal voltage of the machine too much. In Fig. 6.9 the magnetizing inductance is presented as a function of the applied stator flux.

Table 6.3: No load test of MK171012-AA at 40Hz.

Voltage (V)	Current (A)	Flux (p.u.)	L_M (H)
95,5	5,26	0.3140	0,04119
142,8	7,85	0.4695	0,0415
189,6	10,67	0.6234	0,0406
236,5	13,77	0.7776	0,0393
283,5	17,93	0.9321	0,0362
302,5	20,16	0.9946	0,0343
321,4	22,95	1.0567	0,0321
340,2	26,41	1.1185	0,0295
359,5	30,85	1.1820	0,0267
368,8	33,40	1.2126	0,0253
378,3	36,30	1.2438	0,0239
387,8	39,50	1.2750	0,0225
397,3	43,19	1.3063	0,0211
406,6	47,34	1.3369	0,0197

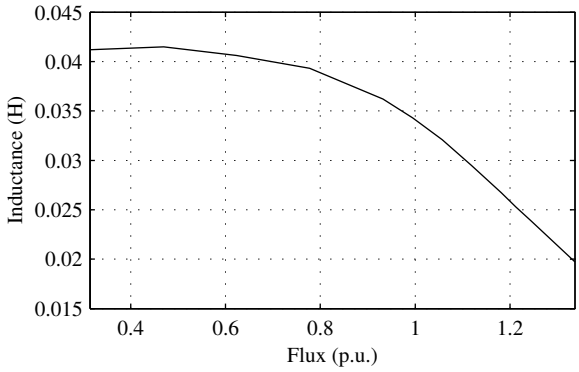

Figure 6.9: The magnetizing inductance as a function of the flux.

It can be noted in the table above that the magnetizing inductance varies with the applied stator flux. However, as a severe fault occurs, a very small amount of the short circuit current will run through the magnetizing inductance. In Fig. 6.10 and Fig. 6.11 the short circuit parameters of the Γ-model are presented using measurement where a fixed (nominal) and a variable magnetizing inductance has been used.

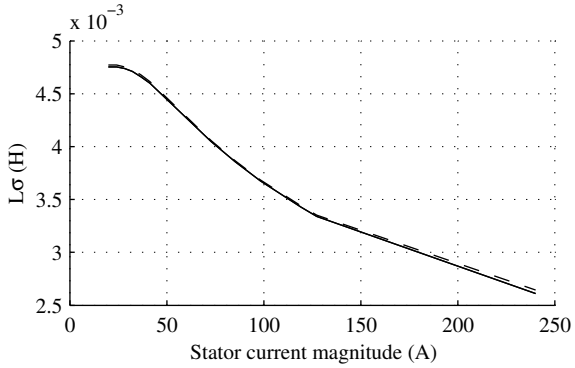

Figure 6.10: The rotor inductance of the Γ-model at a fixed magnetizing inductance according to Table 6.1 (solid) and a varying magnetizing inductance according to Table 6.3 (dashed).

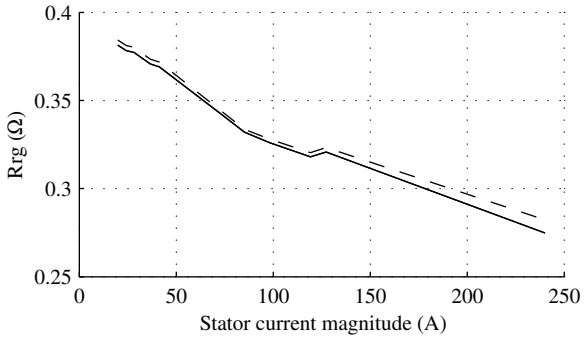

Figure 6.11: The rotor resistance of the Γ-model at a fixed magnetizing inductance according to Table 6.1 (solid) and a varying magnetizing inductance according to Table 6.3 (dashed).

From Fig. 6.10 and Fig. 6.11 it can be observed that the importance of accounting for a variable magnetizing inductance when determining the short circuit parameters of the induction machine is very low.

6.1.2 Locked Rotor Test

The manufacturer general parameters do not imply any consideration to the varying character of the rotor parameters with respect to the frequency or the current. A detailed data sheet from the manufacturer may be available sometimes, which opens up the possibility to at least roughly incorporate for saturation of the leakage flux path and skin effect without performing extensive measurements. In this thesis however, locked-rotor tests at both different frequencies and voltage levels have been performed.

Skin Effect

Considering the skin effect, the influence on the stator parameters are not as large as the influence on the rotor parameters. The stator conductors are relatively thin (approximately 1.9 mm^2 for the 15kW induction machine), and the stator resistance is not affected by the skin effect around 50 Hz and below. This is related to the penetration depth of the magnetic field, into the current carrying conductors and accordingly the stator resistance is kept constant.

The skin depth can be calculated according to [3]

$$\delta = \frac{1}{\sqrt{\pi f \mu \sigma}} \tag{6.1}$$

where f is the frequency, μ the permeability ($\mu = \mu_0 \mu_r$, where $\mu_0 = 4\pi^{-7}$) and σ the conductivity of the conductor material. The permeability and the conductivity for the two most common conductor materials and iron are presented in Table 6.4.

Table 6.4: Skin depths (mm) of various materials.

Material	μ_r	σ
Copper	~ 1	$59{,}6 \cdot 10^6$ mΩ
Aluminum	~ 1	$37,7 \cdot 10^6$ mΩ
Iron	$\sim 10^3$	$10{,}3 \cdot 10^6$ mΩ

In Table 6.5 the different skin depths of copper, aluminium and iron is presented calculations are made using (6.1) and the values according to the table above.

Table 6.5: Skin depths (mm) of various materials.

Material	10Hz	50Hz	100Hz
Aluminum	25,9	11,6	8,2
Copper	20,6	9,2	6,5
Iron	1,57	0,70	0,49

Saturation

A good way to illustrate saturation is the B-H curve, Fig. 6.12, which shows the effect of applying a magnetic field to un-magnetized iron. The magnetizing curve starts at the origin (0,0) and increases linearly as the magnetic field magnetizes the iron (observe that the hysteresis has been neglected in the figure).

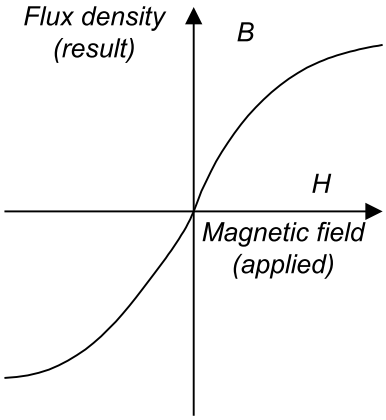

Figure 6.12: B-H curve illustrating the phenomena of saturation.

Eventually, however, all the magnetic domains align with the applied field, and the curve flattens out as the iron becomes magnetically saturated. This is what happens as the current running through the conductors increase. The increasing magnetic field around the conductors saturates the iron around the rotor slots of the machine.

6.1.3 Rotor Parameter determination

With the knowledge of the stator resistance, the magnetizing inductance and the no-load inductance, the leakage inductance as well as the rotor resistance for the Γ-model can be determined using equations (5.35) and (5.36). Table 6.6 and 6.7 presents the leakage inductance (which is the same as the rotor leakage-inductance for the Γ-model), (L_σ) and the rotor resistance (R_{rg}), from the locked rotor tests at different current and frequency levels. It can be noted that the parameters vary with frequency as well as with current magnitude.

Table 6.6: $L_\sigma(mH)$ for different frequencies and stator currents (RMS-values).

Hz	60 A	90 A	120 A
10	4.17	3.70	3.36
15	4.16	3.67	3.31
20	4.14	3.66	3.30
30	4.09	3.627	3.27
40	4.06	3.59	3.23
50	4.01	3.55	3.19
60	3.96	3.50	3.13
80	3.83	3.36	3.03
100	3.66	3.18	2.92

Table 6.7: $R_{rg}(\Omega)$ for different frequencies and stator currents(RMS-values).

Hz	60 A	90 A	120 A
10	0.210	0.202	0.197
15	0.218	0.209	0.208
20	0.229	0.229	0.212
30	0.250	0.246	0.231
40	0.295	0.278	0.254
50	0.337	0.312	0.303
60	0.384	0.359	0.370
80	0.500	0.505	0.471
100	0.642	0.602	0.596

In Fig. 6.13 and in Fig. 6.14 the values from the tables above are presented in two graphs. It is now easy to identify the changes due to different current levels as well as due to varying frequencies.

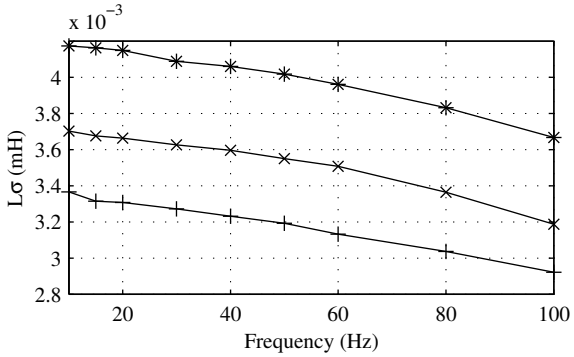

Figure 6.13: The short circuit inductance as a function of frequency at different current levels. The current level is increasing going from the top in the figure to the bottom, $* = 60A$, $\times = 90A$ and $+ = 120A$.

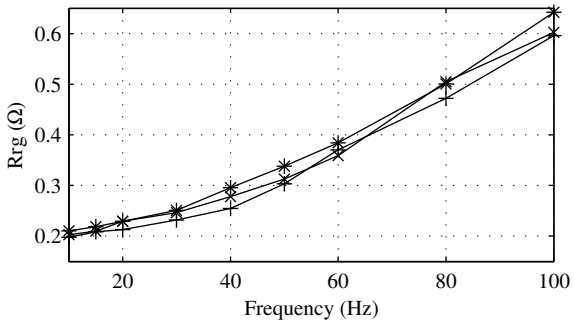

Figure 6.14: The short circuit resistance as a function of frequency at different current levels, $* = 60A$, $\times = 90A$ and $+ = 120A$.

As can be noted in Fig. 6.13, the short circuit inductance does not depend on the frequency very much, whereas the short circuit resistance is highly dependent as can be noted in Fig. 6.14. The current level affects the leakage inductance while it has a very little effect on the resistance.

In Table 6.8 the measured leakage inductance, L_σ, and the rotor resistance, R_{rg}, of the Γ-model is presented as a function of the current magnitude at a fixed frequency of 50Hz, where the effect of saturation is evident.

Table 6.8: Locked rotor test at 50Hz. Voltage source IR and T12

Stator current (A)	L_σ (mH)	R_{rg} (Ω)
6.6	4.433	0.381
13.5	4.520	0.381
17.1	4.542	0.381
23.6	4.554	0.381
30.2	4.534	0.377
37.1	4.477	0.372
44.4	4.386	0.365
59.4	4.017	0.337
90.6	3.551	0.312
120.2	3.194	0.303
197.7	2.831	0.295
244.1	2.616	0.287
280.0	2.498	0.280
301.5	2.433	0.283
310.6	2.411	0.282
395.9	2.248	0.282
429.0	2.164	0.262

To separate the stator and the rotor leakage inductances is practically impossible for a squirrel-cage induction machine, but the distribution between the rotor- and the stator leakage inductance is of minor importance for the dynamic performance of the machine, as long as the total leakage inductance is correct. This emphasizes the use of the Γ-model, which only contains *one* leakage inductance. The Γ-model equivalent circuit is presented in Fig. 6.15.

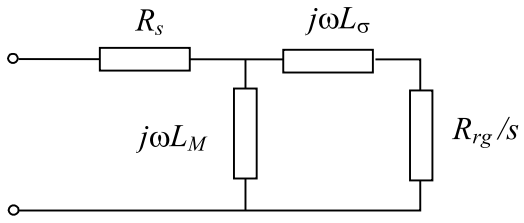

Figure 6.15: Simple equivalent circuit of the Γ-model.

The rotor resistance and the rotor leakage inductance can be calculated for different frequencies resulting in a relationship between those two, which is represents in Fig. 6.16.

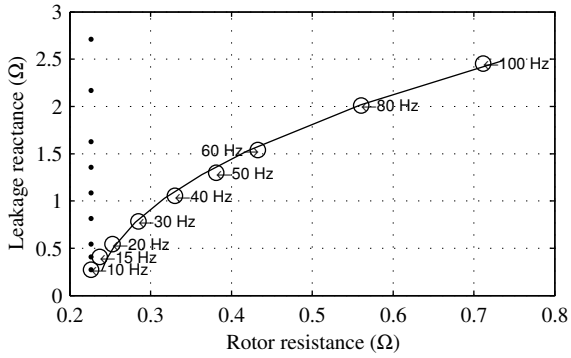

Figure 6.16: Rotor circuit impedance where circles indicate measurements, dots represents the rotor configuration according to Fig. 5.5 and Solid line represents a rotor circuit configuration according to Fig. 5.7.

Both the leakage flux path saturation and the skin effect are both rather simple to account for separately.

To make a rotor equivalent circuit that accounts for both these effects simultaneously seems to be very difficult and perhaps not worthwhile if "cost" is considered with respect to the calculation of the parameters and simulation time when the model is used. In this thesis the following more simple approach has been used and is believed to be adequate.

As these two effects shall be combined *one* current level for which the skin effect shall be represented has been chosen. In our case a medium current level (90A) has been chosen. One advantage, is that the characteristics of the frequency dependent inductance more or less follow the same pattern, regardless of the current level. The total rotor impedance has after the selection of current level been divided into two paths, one that accounts for the leakage flux path saturation and one that accounts for the skin effect.

Fig. 6.17 show the parameters of the rotor circuit, where the two parts, the skin effect representation (to the right) and the representation of the leakage flux path saturation is shown.

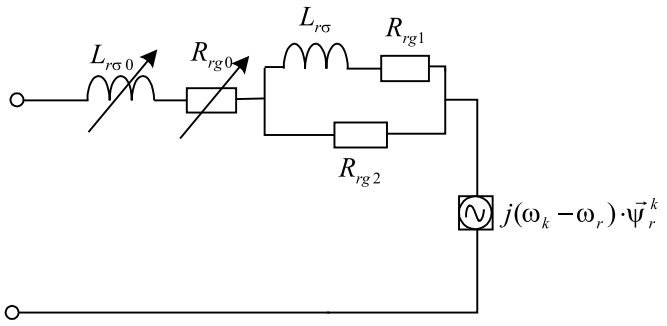

Figure 6.17: The equivalent rotor circuit as the saturation of the leakage flux path and the skin effect are considered.

The resistances are also dependent on the temperature. This factor was eliminated by measurements of the temperature in one of the rotor and the stator windings. By leaving the machine to cool down between the tests the temperature could be held constant. The measured temperature was in this way kept within in a range of 22-27 degrees Celsius.

6.2 Dynamic measurement I - Grid Connection

The measurement set-up for the dynamic measurements were slightly different compared to the previous set-up. It consists of resistances, auto-transformers and the measurement interface, which are the same as for the steady-state measurement set-up. The voltage source however, is only the 50Hz, fixed voltage connections, since the synchronous generator was unable to provide a stable supply voltage during the applied fault conditions. In Fig. 6.18 the measurement set-up for short circuit measurements is presented. As can be noted a short circuit device has been added, which has the possibility to short circuit two or three phases. In Fig. 6.19 a photo of the short circuit device is presented. The different faults were created on the secondary side of the contactor, so for a three phase short circuit fault all three phases were short circuited.

The purpose of the dynamic measurements are to create realistic faults, applied to the terminals of the machine, in order to verify the mathematical models presented in the previous chapters. The primarily applied faults are three phase short circuit faults, which are considered the most severe, and will expose the machine to very high current levels. In the following chapters measurements and simulations will be compared.

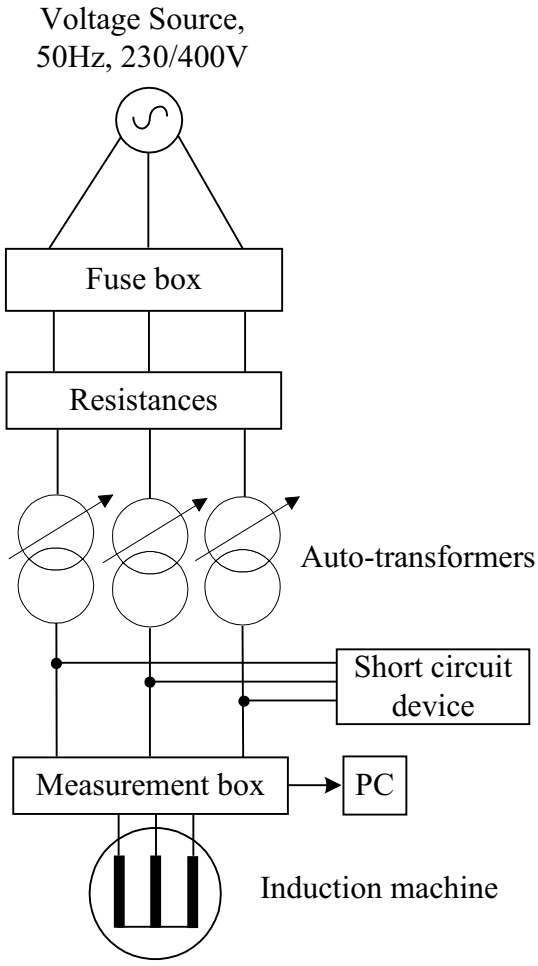

Figure 6.18: The experimental set-up for short circuit measurements.

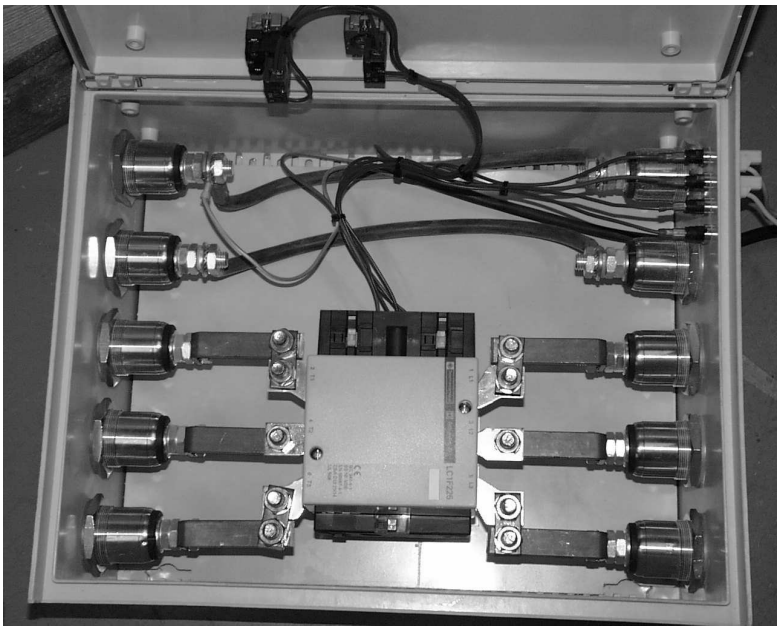

Figure 6.19: The short circuit contactor which is used to short circuit the three phases feeding the induction machine.

6.3 Dynamic Measurement II - Crow-bar operation

Crow-bar operation is related to DFIG systems, which are a bit more sensitive than a fixed speed generator system, since it embraces a converter between the rotor windings and the grid. During fault conditions, the current limitations of the converters can be exceeded. The rotor circuit is then short circuited by means of a crow-bar, in order to protect the converter. At this point of operation the slip-ringed induction machine can be described in the exact same way as the squirrel-cage induction machine, but with a non-natural operating point, initially. The measurements have in this case been performed on a 22kW slip-ringed induction machine.

The experimental set-up for this case, is rather complicated and includes a DC machine with a thyristor rectifier/inverter controlling the torque, a slip-ringed induction machine with resistors emulating the rotor converter and the short circuiting crow-bar. Moreover, a thyristor converter that could generate voltage dips and maintain a stable voltage, regardless of the current level, is used. In this set-up, the current levels had to be kept to a moderate level in contradiction to the previous one, where more brutal tests could be conducted. In Fig. 6.20 the connection is presented and in Fig. 7.15 a picture of the crow-bar set-up is shown.

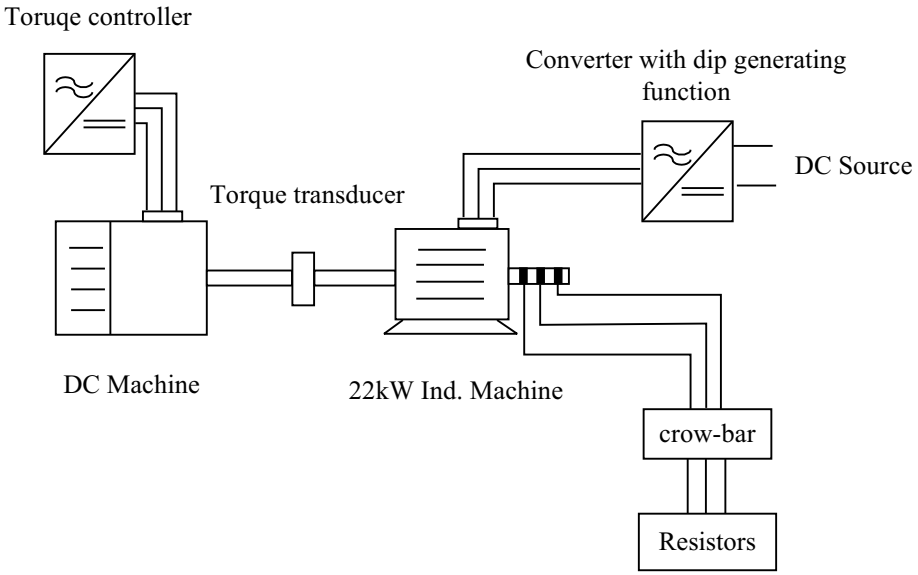

Figure 6.20: A picture of the measurement set-up for measurements of crow-bar operation.

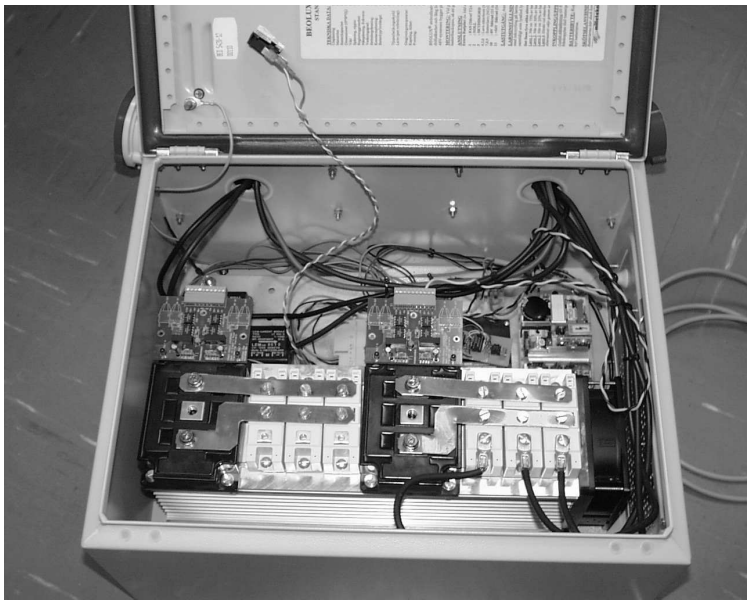

Figure 6.21: The picture shows the crow-bar which short circuits the rotor windings in case of a voltage dip.

The crow-bar consisted of a three-phase diode rectifier with a large IGBT transistor on the dc side. When the rotor current level reached a triggering level, the IGBT was turned on which lead to a short-circuit of the rotor windings.

Chapter 7

Model Verification

All models presented in this thesis can be used for analysis of symmetrical disturbances or faults, although the accuracy of the result varies due to the complexity of the model used. The experimental verification of the models is made comparing simulations and measurements, from locked rotor tests, starts and three-phase short-circuits. The comparisons are made with results from simulations using the traditional fifth order Park model and measured parameters according to the standard locked-rotor and no-load test. Comparisons are also made using the manufacturer general parameters and finally comparisons using the advanced model are presented.

In the following sections, the magnitude of the absolute value of the stator current is usually presented, in order to facilitate the comparisons. The advantage of presenting the stator current magnitude, is that different cases can be compared more easily. The reason for this is that the peak current level, looking at one stator phase current, can differ around 10%, depending on the voltage angle at the time instant of the three-phase short circuit, while the total stator current magnitude is independent of the voltage angle at the time the fault occurs. In Fig. 7.1 the phase current magnitude as a function of the voltage angle, α, is presented.

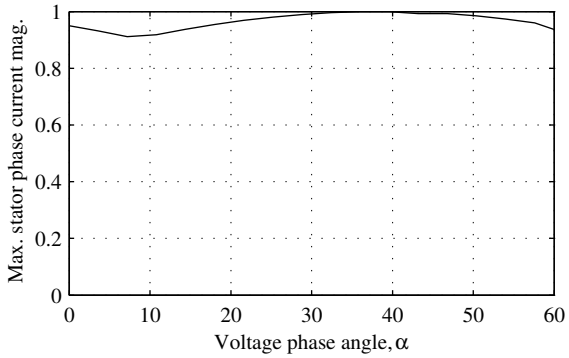

Figure 7.1: The maximum stator phase current magnitude as a function of the voltage angle.

A voltage angle, α, equal to zero corresponds to a three phase short circuit occurring at the time when one of the phase voltages is crossing zero.

7.1 Three Phase Locked Rotor Test

In Fig. 7.2 a locked rotor test at 230 V is presented. The figure shows the stator current magnitude originating from the measurement, the simulation results from using the advanced induction machine model and the same results from using the conventional T-model, when the manufacturer general parameters are used as well as when the parameters are tuned for the specific case. As can be noted, the proposed model predicts excellent result. Worth noticing is the poorly predicted result by the conventional T-model using the manufacturer's parameters, even as the steady-state condition is reached at the end of the time series. An improvement can be made by tuning the parameters of the T-model with respect to the specific current level, i.e. using calculated parameters from a conventional no-load and a specific locked-rotor test made at the specific current level. However, the initial transient processes is still poorly predicted with this method.

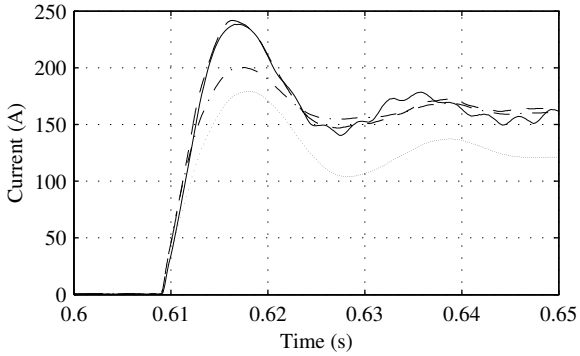

Figure 7.2: Locked-rotor test at 230 V. Solid line show the measurement, dashed line show the advanced model, dashed-dotted line show the T-model with tuned parameters and dotted line show the T-model with the parameters according to standrd manufacturer data.

Fig. 7.3 shows the three-phase currents from the previous case and as can be noted the prediction of the advanced model is as in the previous case very good.

In Fig. 7.4 a locked-rotor test at rated voltage is presented. The same comments that are made for Fig. 7.3, can be made also for this case, but as can be noted the prediction fails slightly as the current raises above 500 A. This is due to limitations of the experimental setup, which made it impossible to have 500A for a time long enough to identify the short circuit parameters. To try to identify the parameters over 500 A, could very well have destroyed the machine as well as other equipment. Higher current levels could perhaps have been obtained by blocking the protection systems

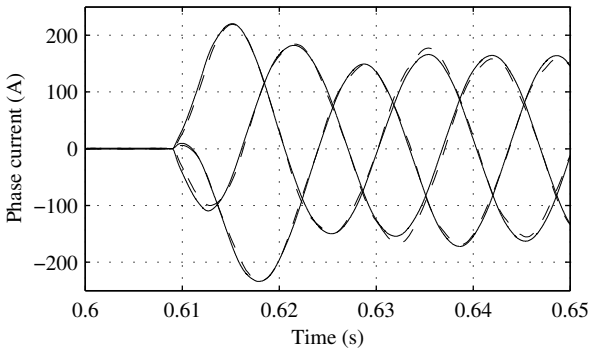

Figure 7.3: Locked-rotor test at 230 V. Solid line show the advanced model and dashed line show the measurement.

and changing to larger fuses in the internal power supply of the laboratory, but was not considered necessary since the modelling strategy proved to work extremely well for the 230V case.

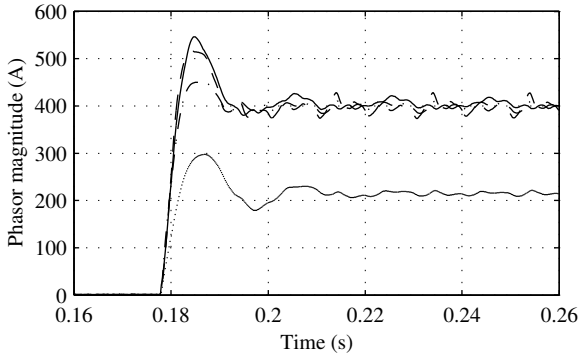

Figure 7.4: Locked-rotor test at 400 V. Solid line show the measurement, dashed line show the advanced model, dashed-dotted line show the T-model with tuned parameters and dotted line show the T-model with the parameters according to manufacturer data.

7.2 Start

Starting the induction machine by connecting it directly to the grid imply that the machine is subjected to a quit high current initially due to the magnetization and acceleration of the rotor. This current has a magnitude in the range of approximately 7 - 10 times rated current. As the machine in this case is started without load, the starting time is quite short and the high current decays rather quickly.

Fig. 7.5 shows the absolute value of the current from a start at 230 V and Fig. 7.6 shows the three-phase currents.

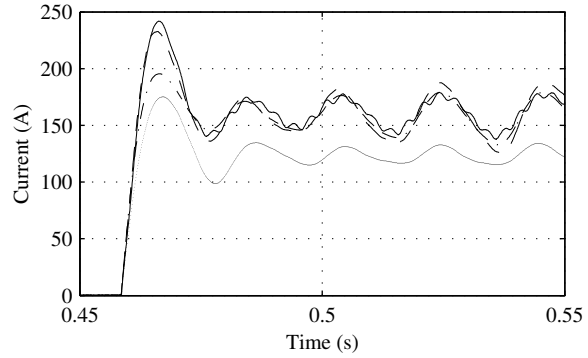

Figure 7.5: A start at 230 V. Solid line show the measurement, dashed line show the advanced model, dashed-dotted line show the T-model with tuned parameters and dotted line show the T-model with the parameters according to manufacturer data.

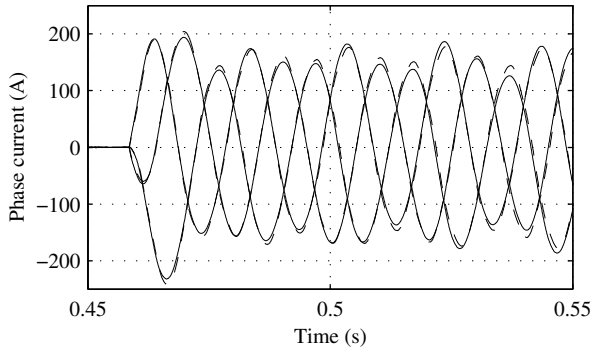

Figure 7.6: A start at 230 V. Solid line show the advanced model and dashed line show the measurement.

In Fig. 7.7 a comparison between the measurements, the conventional T-model, with the manufacturers general parameters and with tuned parameters, as well as the advanced model is presented. It is again evident that an advanced model predicts the currents very well compared to the prediction by the traditional T-model, which does not predict a very good result.

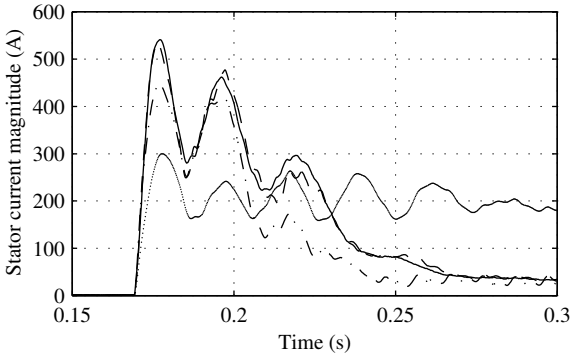

Figure 7.7: Start of the induction machine at rated voltage (400 V). Solid line show the measurement, dashed line show the advanced model, dashed-dotted line show the T-model with tuned parameters and dotted line show the T-model with the parameters according to manufacturer data.

7.3 Three Phase Short Circuit Fault

During a three-phase short circuit the machine is de-energized and subjected to currents with a magnitude in the same range, as the machine is subjected to at a start (direct start).

In Fig. 7.8 a three-phase short circuit is presented at 230 V. It shows the prediction by the advanced model and the T-model with the parameters according to the manufacturer and as well as the parameters adjusted for the specific case.

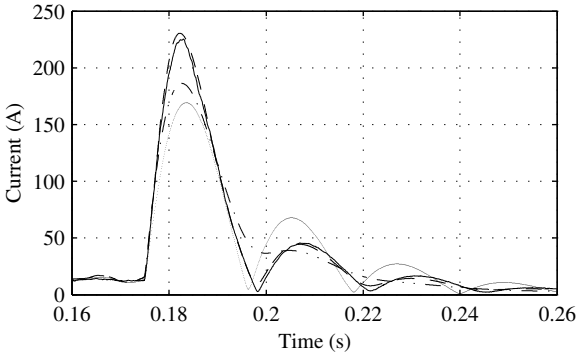

Figure 7.8: A three phase short circuit test at 230 V. Solid line show the measurement, dashed line show the advanced model, dashed-dotted line show the T-model with tuned parameters and dotted line show the T-model with the parameters according to manufacturer data.

Fig. 7.9 shows the same case, but presents the three-phase currents.

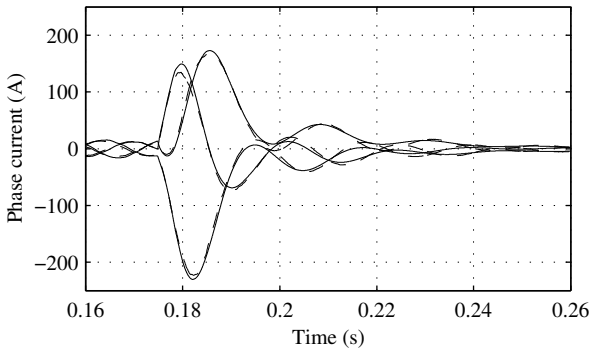

Figure 7.9: Short circuit at 230 V. Solid line show the advanced model and dashed line show the measurement.

To really verify the model presented in this thesis, the machine has been subjected to full or rated voltage short circuits. In Fig. 7.10 the absolute value of the current predicted by the advanced model and the T-model. For the T-model, two sets of parameters have been used; The manufacturer general parameters and a set of parameters adjusted to fit this specific case (The parameters given from a full-voltage locked-rotor test).

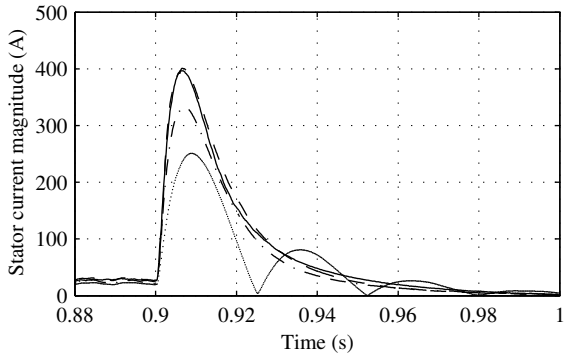

Figure 7.10: Short circuit fault applied on the 15kW squirrel-cage induction machine at 400 V. Solid line show the measurement, dashed line show the advanced model, dashed-dotted line show the T-model with tuned parameters and dotted line show the T-model with the parameters according to manufacturer data.

In Fig. 7.11 the three-phase currents are presented for the same case.

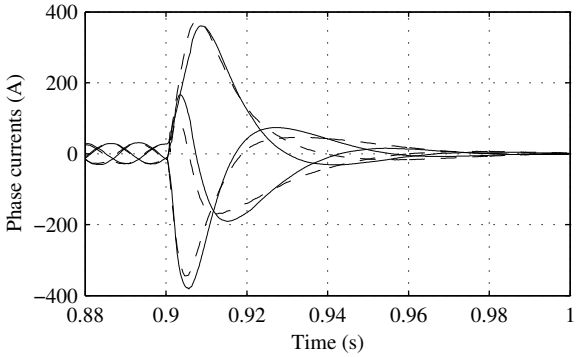

Figure 7.11: Short circuit fault applied on the 15kW squirrel-cage induction machine at 400 V. Solid line shows the advanced model and dashed line the measurement.

As can be noted in the above presented comparisons, the agreement between measurements and the advanced model is excellent.

7.3.1 IEC 909 Comparison

In Chapter 4 the short circuit calculation procedure for induction machine was presented. The parameters according to the manufacturer was used and the initial short circuit current as well as the peak short circuit current were calculated. The peak short current which is the highest current level during a short circuit and the absolute highest value can be seen during three phase short circuits.

For the 15kW squirrel-cage induction machine the peak short circuit current was calculated to 451A, which is to be compared with peak current value according to the measurement and the simulation in Fig. 7.11. The measurement and the simulation shows a result of approximately 370A, so the IEC standard provides a somewhat high result. This is of course better than if the result would be to low, but as large generators and wind farms are put up and used for calculating the fault currents, this can be associated with high costs. The dimensioning of substations are dependent on the short circuit currents and going from one short circuit level to a higher one can be very expensive. Circuit breakers, fuses, busbars and all other equipment must be able to withstand the forces due to a three phase short circuit.

7.4 DFIG-System

When severe disturbances are considered, the fault response of a doubly-fed induction machine is similar to the response of the short-circuited induction machine, but it also be worse, depending on the point of operation at the time before the fault and the crow bar operation. If the current limitation of the inverter connected to the rotor circuit of a slip-ringed induction machine is exceeded, the rotor windings are short circuited by a crow-bar device, which protects the rotor inverter from over voltages. For smaller grid

disturbances however, the response of the DFIG-system is to high extent determined by the control system and its ability to counteract smaller voltage dips [1]. Fig. 7.12 presents a scheme of the DFIG system.

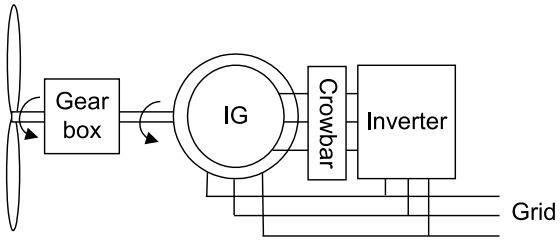

Figure 7.12: Setup of the experimental DFIG system for disturbance analysis.

7.4.1 Short circuit parameters

The parameter variation due to skin effect and the leakage flux path saturation of the 22kW slip-ringed induction machine have not been taken into consideration in the simulations presented in this section. However, the parameters vary in the same way as for the squirrel-cage induction machine. A difference is however that the skin effect is much less dominant in the slip-ringed induction machine due to the wounded rotor.

Fig. 7.13 presents the resistances as a function of frequency for the two different machines.

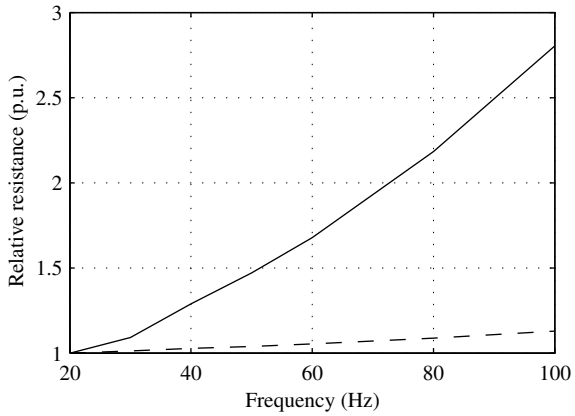

Figure 7.13: The resistances as a function of frequency for the slip-ringed induction machine (dashed) and the squirrel-cage induction machine (solid).

7.4.2 Crow-bar Operation

During severe fault conditions or disturbances, where the limitations of the rotor converter are exceeded, a protective circuit is activated and a crow-bar short circuits the rotor conductors. The operation of the crow-bar imply that the slip-ringed induction

machine temporarily is changed into a short circuited induction machine.

In Fig. 7.14 the three phase voltages during a voltage drop of approximately 37%, which forces the crow-bar to operate, is presented.

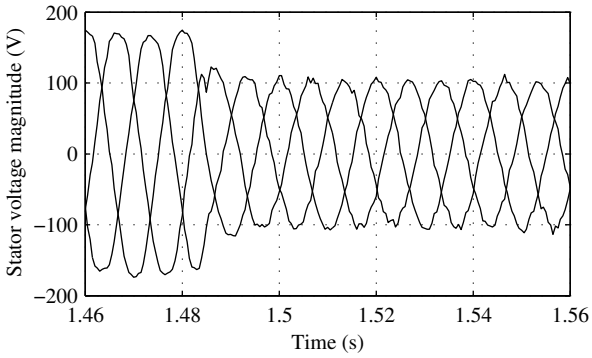

Figure 7.14: Three phase voltages during a crow-bar operation of the 22kW slip-ringed induction machine.

In Fig. 7.15 simulations and measurements of the currents for the same case is presented.

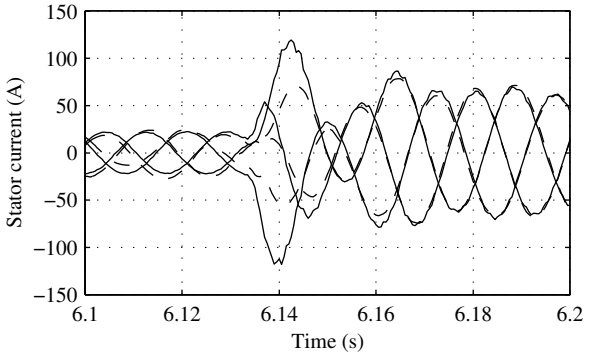

Figure 7.15: Three phase currents during a crow-bar operation of the 22kW slip-ringed induction machine. Solid lines presents measurements and dashed lines presents simulations.

The resemblance between measurement and simulations are during "steady state" operation quite satisfactory, but during the most transient period, the model fails to predict the stator currents accurately. However, in this case the manufacturers parameters have been used and the skin effect as well as the effect of leakage flux path saturation have been neglected, which more or less explains the difference between measurements and simulations in Fig. 7.15.

7.4.3 Field measurements

In Fig. 7.16 a measurement of a short circuit on a doubly-fed induction generator wind turbine is presented. The grid disturbance is so large that the crow-bar has to operate. After the crow-bar operation, the slip-ringed induction generator behaves in the same way as a squirrel-cage induction generator and after 40ms the wind turbine is disconnected from the grid.

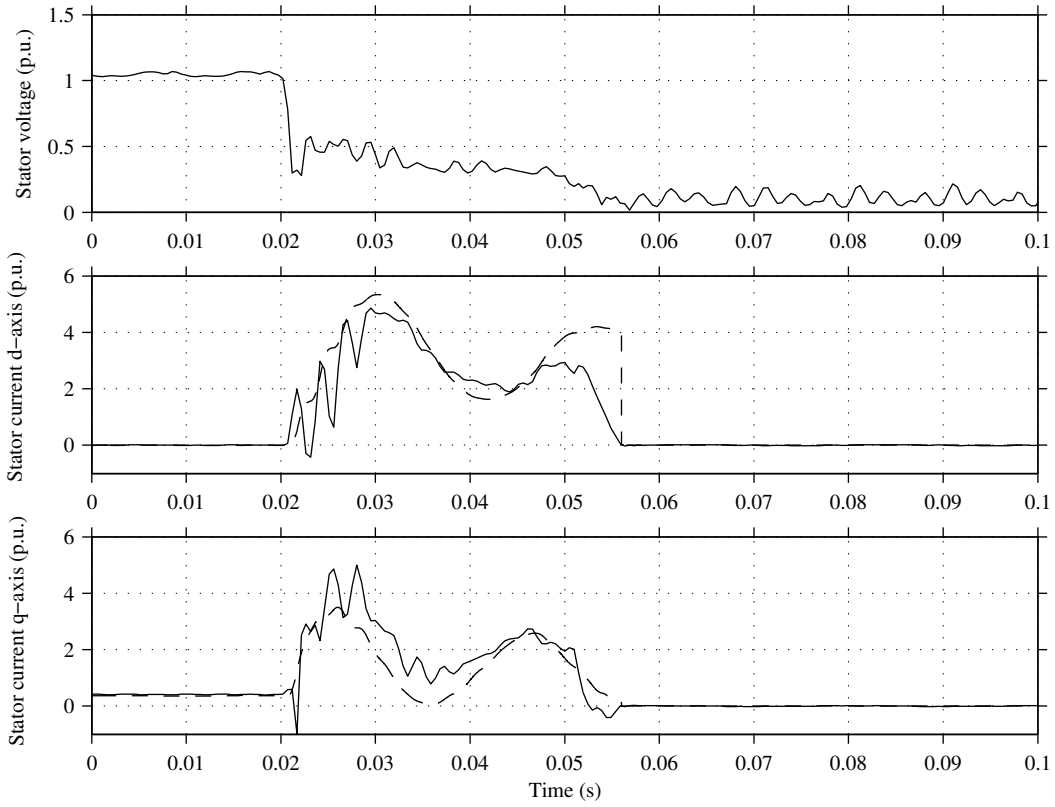

Figure 7.16: A three phase short circuit of a 850kW wind turbine doubly-fed induction generator. Solid lines show measurements and dashed lines show simulations.

The parameters of this generator was not known, but have been approximated by using parameters from a generator with the same rated power as the generator in question. The varying character of the short circuit parameters due saturation, have been taken into account by considering the variations according to the prior measurements on the 15kW induction machine. The skin effect has been ignored since the DFIG-system has a wounded rotor. It can be noted that the agreement is quite good.

7.5 Unsymmetrical Faults

As been mention in the previous chapters, a suitable model for fault current prediction depends on the specific application of the generator. For wind turbine applications,

the generator is normally connected in delta, which imply a nonexistent neutral point and that any of the presented models can be used for fault current prediction. In case the generators are connected in wye and the star point is connected to the neutral conductor, this may imply that there is a possibility of having a current running through the neutral conductor (zero sequence component).

In this section, the measurements have been done at rather low voltage levels in order to avoid leakage flux saturation, which already has been investigated in the previous chapter.

7.5.1 One Phase to Ground Fault

A one phase to ground fault imply that one of the three phase conductors is connected to ground, most likely via an impedance. The impedance of the short-circuit as well as the impedance of the neutral conductor has in the following simulations been neglected. This type of fault would not occur in a wind turbine, since the neutral point would not be connected to the generator. Moreover, the result would also be affected by how the electrical grid supplying the wind turbine is grounded. If the fault occurred on the high voltage side of the feeding transformer, nothing would probably happen, since the network usually is grounded through a rather high impedance.

However, this case is shown to demonstrate the response due to asymmetrical faults. In order to focus on the positive and the negative sequence, the zero-sequence current has been removed from the plot.

In Fig. 7.17 the results from a one-phase to neutral short circuit together with the result obtained form the three-phase model are presented, as the zero sequence current component has been subtracted from the calculated as well as the measured result. The agreement is fairly good.

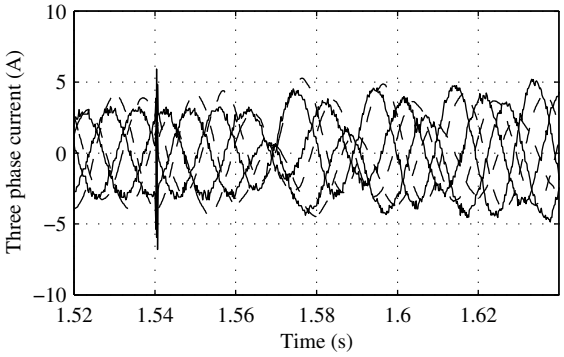

Figure 7.17: A one phase to ground short circuit. Measurements (Solid) and simulations (Dashed) using the three-phase model are presented, as the zero seq. component is neglected.

7.5.2 Two Phase to Ground Fault

This case imply that two phases are short circuited and connected to ground. The same comments as for the previous case can be made. The measurements and the simulations are presented in Fig. 7.18.

The zero sequence component is once again neglected and it can be observed from the figure that the agreement between the measurement and the simulations is very good.

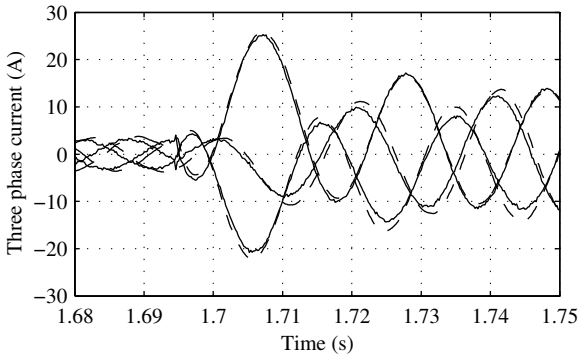

Figure 7.18: A two phase to ground short circuit. Measurement (Solid) and simulation (Dashed) are presented using the three-phase model, as the zero seq. component is neglected.

7.5.3 Two Phase Short Circuit

The two phase short circuit does not imply any interconnection between the ground or the neutral conductor and does accordingly not involve any zero sequence components.

The three-phase model presents an accurate result as can be observed in Fig. 7.19

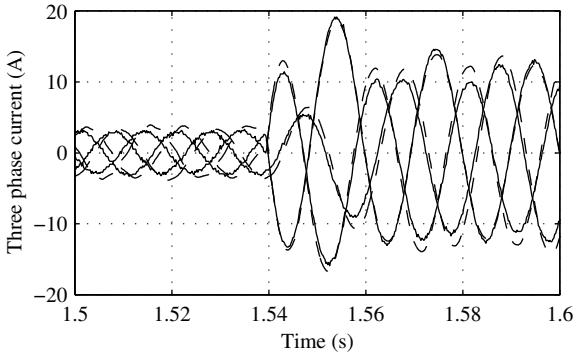

Figure 7.19: A two phase short circuit. Measurements (Solid) and simulations (Dashed) using the three-phase model.

Chapter 8

Conclusion

The thesis has focused on creating a general model of the induction machine, the squirrel cage as well as the slip-ringed induction machine. The main objective for use of the model is fault current prediction during severe fault conditions. The thesis presents how the skin effect and the effect of saturation of the leakage flux path can be accounted for. Extensive measurement series have been made in order to determine the needed parameters.

Comparisons between the measurements and different more or less advanced models, for prediction of the fault currents due to symmetrical faults is presented. The advanced model, that takes the skin effect and the saturation of the leakage flux path into saturation shows excellent results. A comparison between measurement and simulation, when the rotor windings are short circuited by a crow-bar, is made for the slip-ringed induction machine, which also show a rather good agreement. The result is not excellent due to that the saturation of the leakage flux path was not known and thus not incorporated in this case. Further, unsymmetrical fault conditions are treated to some extent and are presented together with simulations. The resemblance in these cases are very good.

The short circuited induction machine and the slip-ringed induction machine behave in a similar manner, when heavy fault conditions are considered, since the rotor windings of the slip-ringed induction machine are short circuited almost immediately after the fault has occurred. In fact, if a crowbar action has been initiated for the DFIG wind turbine system, it takes a lot of reactive power from the grid and it must be disconnected as soon as possible, which occurs after about 40ms. The slip-ringed induction machine can then be described in the exact same way as the squirrel-cage induction machine. For short-circuit fault current prediction, the same mathematical models can be used to represent the squirrel cage as well as the slip-ringed induction machine.

References

[1] Petersson Andreas. Analyis, modeling and control of doubly-fed induction generators for wind turbines. Department of Electric Power Engineering, Chalmers University of Thechnology, Göteborg, Sweden, 2003.

[2] Adkins B. and Harley R. *The general theory of alternating current machines: Application to practical problems*. Chapman and Hall, London, 1975.

[3] K. Cheng David. *Field and Wave Electromagnetics*. Addison-Wesley Publishing Company, second edition, 1998.

[4] Stojanovic Dobivoje, Vaselinovic Miroslav, Mitrovic Nebojsa, and Korunovic Lidja. Calculations and analysis of induction motors impact on short-circuit current. *10 th Medeterranean Electromechanicl Conference, MEIeCon 2000*, Vol. III:1076–1079, 2000.

[5] Cortinas D. and Juston P. Assessing the impact of dispersed generation on medium voltage networks: Analysis methods. *IEEE Power Tech '99 Conference*, Aug., 1999.

[6] Slemon G.R. Modelling of induction machines for electric drives. *IEEE Transaction on Industry Application*, Vol. 25(No. 6), 1989. Finns inte i artikelpärmen.

[7] Crossley P.A. Jenkins N. Haslam, S.J. Design and evaluation of a wind farm protection relay. *IEE Proc.-Gener. Transmis. Distrib.*, 146(1):37–44, January 1999.

[8] Lorenzen H.W. Der einfluss der stromfördrengung auf die erzwungenen pendulengen von asynchronmachinen. *ETZ-A*, 88(18):445–451, 1967.

[9] IEC 909 International Electrotechnical Comminssion. Short-circuit current calculaion in three-phase a.c. systems. Publication 909:1988, First edition, 1988.

[10] interviews.

[11] Luomi Jorma. *Transient Phenomena in Electrical Machines*. Department of Electric Power Engineering, Chalmers University of Technology, Göteborg, Sweden 1997.

[12] Bollen Mathias. *On Travelling-Wave-Bassed Protection of High-Voltage Networks.* PhD thesis, Eindhoven University of Technology, Faculty of Electrical Engineering, 1989.

[13] Mohan Ned. *Electric Drives, An Integrative Approach.* MNPERE, Minneapolis, the 2003 edition edition.

[14] Harnefors L. Nee, H.P. Control of variable-speed drives. Electrical Machines and Power Electronics, Department of Electrical Engineering, Stockholm, Sweden, 2000.

[15] Fountas N. A. and Hatziargyriou N. D. Estimation of induction motor parameters for dynamic analysis. In *Proceedings of the 7th Mediterranean Electrotechnical Conference - MELECON. Part 3 (of 3)*, Mediterranean Electrotechnical Conference - MELECON, pages 1263–1266, Antalya Turkey, 1994. IEEE Piscataway NJ USA. 9 Refs. IEEE; Middle East Technical University; Bilkent University; Chamber of Electrical Engineers of Turkey.

[16] Thorsen O. V. and Dalva M. Model for simulation of induction motors with parameter determination and examples of application. In *Proceedings of the 1997 IEEE International Electric Machines and Drives Conference, IEMDC*, IEEE International Electric Machines and Drives Conference Record, IEMDC, pages MB1 3.1–3.3, Milwaukee Wi USA, 1997. IEEE Piscataway NJ USA. 7 Refs. IEEE.

[17] Kovacs P.K. *Transient phenomena in electrical machines.* Elsavier, Budapest, 1984.

[18] Healey Russell C., Williamson Stephen, and Smith Alexander C. Improved cage rotor models for vector controlled induction motors. *IEEE Transactions on Industry Applications*, 31(4):812–822, 1995.

[19] Yamamura S. *AC Motors for High-Performance Applications. Analysis and Control.* Marcel Dekker, Inc. New York, 1986.

[20] Thiringer Torbjörn. *Measurements and modelling of low-frequency disturbances in electricl machines.* Technical report, Chalmers University of Technology, Sweden, 1996.

[21] Deleroi W. Berücksichtigung der eisensättigung für dynamische betriebszustände. *Archiv für Electrotechnik*, 54:31–42, 1970.

[22] Maljkovic Zlatko, Cettolo Mirko, and Pavlica Milutin. Induction motor's contribution to short-circuit current. pages 354–356, 1999.

[23] SS 4211811. Swedish Standard, 1989. edition 3.

[24] Starkströmsföreskrifterna, (swedish). ELSÄK-FS, 1994:7.

[25] Anslutning av mindre produktions-anläggningar till elnätet, (swedish). Sveriges Elleveratörer.

Appendix A

Nomenclature

$WESC$ Wind energy conversion system
$DFIG$ Doubly-fed induction genertor
$SFIG$ Singly-fed generator system
$EMSM$ Electric magnetized synchronous machine
$PMSM$ Permanent magnet synchronous machine
IG Induction generator
SG Synchronous generator
T Time constant
T_e Electromechanical torque
T_m Mechanical torque
t Time
j Imaginary part
P_n Rated power
P_e Electrical power
P_m Mechanical power
P Active power
Q Reactive power
S Apparent power
B Flux density
H Magnetic field
f frequency
$cos\phi$ Power factor
n speed
a Operator equal to $e^{2\pi/3}$
K Transformation factor
k Arbitrary reference frame
J Inertia
p Number of pole pairs
s slip, stationary reference frame, stationary reference frame
Re Real part

Im Imaginary part
ω_k Angular speed of an arbitrary reference frame
ω_r Angular speed of the rotor reference frame
Ω_m Angular mechanical speed of the generator shaft
U_n Rated voltage
U_{DC} DC voltage
$\hat{u}$ Peak voltage value
$u_{rs,st}$ Stator Line to line voltages
u_α Real part of the voltage vector for the two-axis model
u_β Imaginary part of the voltage vector for the two-axis model
u_0 Zero sequence voltage component
$u_{sa,a}$ Stator voltage in phase a
$u_{sb,b}$ Stator voltage in phase b
$u_{sc,c}$ Stator voltage in phase c
$\vec{u}^s$ Voltage vector in a stationary reference frame
$\vec{u}^k$ Voltage vector in a arbitrary reference frame
$\vec{u}_s^k$ Stator voltage vector of an arbitrary reference frame
$\vec{u}_s^s$ Stator voltage vector in a stationary reference frame
u_s^x Real part of the stator voltage vector in a arbitrary reference frame
u_s^y Imaginary part of the stator voltage vector in a arbitrary reference frame
u_{ra} Rotor voltage in phase a
u_{rb} Rotor voltage in phase b
u_{rc} Rotor voltage in phase c
$u_{ab,bc}$ Rotor Line to line voltages
$\vec{u}_r^k$ Rotor voltage vector of an arbitrary reference frame
u_r^x Real part of the rotor voltage vector in a arbitrary reference frame
u_r^y Imaginary part of the rotor voltage vector in a arbitrary reference frame
$\vec{u}_{sk}^k$ Voltage vector of the skin effect branch of an arbitrary reference frame
u_{sk}^x Real part of the skin effect branch voltage vector in a arbitrary reference frame
u_{sk}^y Imaginary part of the skin effect branch voltage vector in a arbitrary reference frame
I_n Rated current
I_{DC} DC current
$i_{x,y,z}$ Phase currents for either the stator or the rotor
i_{sc} Total short circuit current
i_{dc} Direct current
i_{ac} Alternative current
I_p peak short circuit current
$I_{sc}^{''}$ Initial short circuit current
$i_{sa,a}$ Stator current in phase a
$i_{sb,b}$ Stator current in phase b

$i_{sc,c}$ Stator current in phase c
$\vec{i}_{res}$ Resultant current vector
I_{LR} Locked rotor current
$\vec{i}_s^k$ Stator current vector of an arbitrary reference frame
$\vec{i}_s^s$ Stator current vector in a stationary reference frame
i_s^x Real part of the stator current vector in a arbitrary reference frame
i_s^y Imaginary part of the stator current vector in a arbitrary reference frame
i_{ra} Rotor current in phase a
i_{rb} Rotor current in phase b
i_{rc} Rotor current in phase c
$\vec{i}_r^k$ Rotor current vector of an arbitrary reference frame
i_r^x Real part of the rotor current vector in a arbitrary reference frame
i_r^y Imaginary part of the rotor current vector in a arbitrary reference frame
$\vec{i}_{sk}^k$ Current vector of the skin effect branch of an arbitrary reference frame
i_{sk}^x Real part of the skin effect branch current vector in a arbitrary reference frame
i_{sk}^y Imaginary part of the skin effect branch current vector in a arbitrary reference frame
$\psi_{sa,a}$ Stator flux in phase a
ψ_{sb} Stator flux in phase b
ψ_{sc} Stator flux in phase c
$\vec{\psi}_s^k$ Stator flux linkage for an arbitrary reference frame
$\vec{\psi}_s^s$ Stator flux linkage vector in a stationary reference frame
$\vec{\psi}_r^k$ Rotor flux linkage for an arbitrary reference frame
$\vec{\psi}_{sk}^k$ Flux linkage in the skin effect branch for an arbitrary reference frame
L inductance
$L_{s\lambda}$ Stator leakage inductance of the T-model
$L_{r\lambda}$ Rotor leakage inductance of the T-model
L_m Magnetizing inductance of the T-model
L_s Stator inductance
L_r Rotor inductance
L_σ Leakage inductance of the Γ-model
L_M Magnetizing inductance of the Γ-model
$L_{r\sigma 0}$ Current dependent rotor inductance of the detailed model
$L_{r\sigma}$ Inductance in the skin effect branch of the detailed model
L_h Main inductance of a winding
$L_{r\sigma 0}^{x,y,xy}$ Result from derivation of the product $L_{r\sigma 0}\vec{i}_r^{x,y}$
$L_{\sigma 0}^{A,B,C}$ Result from derivation of the product $L_{r\sigma 0}\vec{i}_r^{a,b,c}$
M Mutual inductance
X Reactance
X_{LR} Locked rotor reactance
X_M Magnetizing reactance of the Γ-model
X_σ Rotor reactance of the Γ-model

X_0 No load reactance
$X_{s\lambda}$ Stator leakage reactance of the T-model
X_m Magnetizing reactance of the T-model
R Resistance
R_s Stator resistance
R_r Rotor resistance of the T-model
R_{rg} Rotor resistance of the Γ-model
R_{rg0} Current dependent rotor inductance of the detailed model
$R_{rg1,rg2}$ Resistances in the skin effect branch of the detailed model
R_{LR} Locked rotor resistance
R'_{LR} Locked rotor resistance subtracted by the stator resistance
R_m Magnetizing resistance
α Voltage angle at the time of a short circuit
φ Angle between voltage and current
ω Synchronous angular speed
κ Peak current factor
δ Angle between the real axis and a vector component, skin depth
ν_k Angle between the real axis in a arbitrary reference frame and a stationary reference frame
ϑ Angle between two phase windings
γ Angle between the rotor and the stator windings
μ Permability
σ Conductivity
Z Complex impedance
Z_{LR} Locked rotor impedance

Appendix B

Publications

Helmer, M., "Optimized Size of Wind Power Plant Transformer", NWPC, Trondheim, 13-14/3, 2000.

Larsson, Å., Helmer, M., Johansson, C., "Parallella Transformatorer för Vindkraftverk", Elforskrapport, nr.00:25, 2000.

Helmer, M., "Optimized Size of Wind Power Plant Transformer and Parallell Operation", Wind Power for the 21^{th} Century, Kassel, 25-27/9, 2000.

Helmer, M., "Protection and Influences of Wind Farms from Wind Turbine and Grid Point of View", EWEC, Köpenhamn, 2-6/7, 2001

Carlson, O., Helmer, M., Liljegren, C., "Analys av havererade asynkrongeneratorer", Elforsk informerar, VINDKRAFT-4 / 01.

Helmer, M., "Vindkraftparker - Skydds och nätintegreringsaspekter", Elforsk informerar, VINDKRAFT-3 / 01.

Helmer, M., Thiringer, T., "An Improved Model of Induction Machines for Accurate Predictions of Wind Generator Line Short Circuit Currents", EPE 2003, 10^th European Conference on Power Electronics and Applications, Toulouse, France.